Eur. Phys. J. A **4**, 115–145 (1999)

THE EUROPEAN PHYSICAL JOURNAL A

High-spin shell-model states near ^{56}Ni

D. Rudolph[1], C. Baktash[2], M.J. Brinkman[2], M. Devlin[3], H.-Q. Jin[4,a], D.R. LaFosse[3b], L.L. Riedinger[4], D.G. Sarantites[3], C.-H. Yu[2]

[1] Department of Physics, Lund University, S-22100 Lund, Sweden
[2] Physics Division, Oak Ridge National Laboratory, Oak Ridge, TN 37831, USA
[3] Chemistry Department, Washington University, St. Louis, MO 63130, USA
[4] Department of Physics, University of Tennessee, Knoxville, TN 37996, USA

Received: 19 September 1998 / Revised version: 27 November 1998
Communicated by D. Schwalm

Abstract. High-spin states of nuclei near doubly magic ^{56}Ni were studied with the reaction ^{28}Si(^{36}Ar,x*pynz*α) at 136 MeV beam energy. The GAMMASPHERE array in conjunction with the 4π charged-particle detector array MICROBALL and neutron detectors were used to detect γ rays in coincidence with evaporated light particles. The resulting extensive decay schemes of ^{54}Fe, ^{54,55}Co, ^{56,57}Ni, and ^{58}Cu are compared to shell model calculations in the fp shell.

PACS. 21.60.Cs Shell model – 23.20.En Angular distribution and correlation measurements – 23.20.Lv Gamma transitions and level energies – 27.40.+z $39 \leq A \leq 58$

1 Introduction

Doubly magic nuclei and their nearby neighbors are uniquely suited to test predictions from (large scale) shell-model calculations. On the one hand spectroscopic data from these nuclei provide essential information for the parameter sets of spherical shell-model calculations, i.e., single-particle energies and two-body matrix-elements. On the other hand they put the most severe constraints on the outcome of such calculations and, consequently, define and relate the effective nuclear forces.

In this paper we present comprehensive new high-spin data for nuclei located in the ^{56}Ni region. While this regime has been studied extensively with light ion induced reactions (see, for example, [1]), barely anything is known regarding their high-spin behavior. Most of the reported decay schemes date back to the mid 1980's, comprising five to ten transitions and reaching up to spins $I \leq 10$ at excitation energies below ~ 7 MeV. In fact, this lack of information is somewhat surprising and contradictive to their significance with respect to effective interactions — even more since they are (and, in principle, have been) readily accessible via heavy-ion induced fusion-evaporation reactions. Indeed, spherical high-spin states could be identified in the $T_z = -1/2$ nucleus ^{55}Ni [2] using the present data set.

Other exciting results of our recently initiated high-spin study of the $A \approx 60$ region include the observation of well- and superdeformed rotational bands in second or third minima of nuclei in the vicinity of ^{56}Ni [3,4]. In some cases the bands could be followed up to their so-called terminating states, i.e., reaching the highest possible angular momenta ($I \approx 30\ \hbar$) for a given configuration [5] at excitation energies in excess of 30 MeV. Most interestingly, however, was the first observation of a prompt discrete proton decay out of the band head of the *well-deformed* ($\beta_2 \approx 0.4$) band in ^{58}Cu linking into a *spherical* state in the daughter nucleus ^{57}Ni [4]. Unlike other (deformed) proton emitters along the proton drip line ($\tau > 10^{-3}$ s) [6–9] this decay has to compete with fast ($\tau \leq 10^{-9}$ s) electromagnetic γ radiation, and constitutes the first observation of prompt particle decay of a state associated with a deformed secondary minimum in the potential. Most recently, a second prompt proton emission was suggested for a superdeformed band in ^{56}Ni itself [10].

Here we concentrate on the extensive results in the first, spherical minimum. A small (preliminary) fraction of these has been presented in the proceedings of the 1997 conference on Nucleon-Nucleon interactions [11]. In Sect. 2 we describe the experiment and procedures employed in the course of the data analysis. The results for ^{54}Fe, ^{54,55}Co, ^{56,57}Ni, and ^{58}Cu are presented in Subsects. 2a to 2f. In Sect. 3 the data are compared to shell-model calculations in the $1f$-$2p$ shell with up to two particles crossing the spherical shell gap at particle number $N = Z = 28$.

[a] *Present address:* NASA Ames Research Center, Moffett Field, CA 94035
[b] *Present address:* Department of Physics, SUNY Stony Brook, Stony Brook, NY 11794

2 Experimental procedures and results

The experiment was performed at the 88-Inch Cyclotron at the Lawrence Berkeley National Laboratory. High-spin states in various residual nuclei were populated using the fusion-evaporation reaction ^{28}Si(^{36}Ar,x$pynz\alpha$) at 143 MeV beam energy. A 0.42 mg/cm^2 thin target layer of 99.1 % enriched ^{28}Si was evaporated onto a 0.9 mg/cm^2 Tantalum support foil. This foil faced the beam which lead to a reduction of some 7 MeV in the beam energy. At the time of the experiment the GAMMASPHERE array [12] comprised 82 Germanium detectors. The prompt γ radiation was measured in prompt coincidence with the evaporated light particles to provide reaction channel selection. The charged particles were detected in the 4π CsI ball MICROBALL [13] while neutrons were measured in fifteen liquid scintillator neutron detectors. These replaced the Ge-detectors located in the three most forward (beam direction) rings of GAMMASPHERE. The event trigger required the detection of either three γ rays or two γ rays and one neutron. A total of 2×10^9 events were collected in four days of beam time. We also collected several hours data using a 136 MeV ^{36}Ar beam impinging onto a 11.7 mg/cm^2 Ta-backed 0.44 mg/cm^2 ^{28}Si target layer. Since the recoils were stopped in the backing this data set allowed (for reaction channels having cross-sections in excess of a few millibarn) for the identification of isomers in the nanosecond regime and the evaluation of more precise angular distribution and correlation coefficients (see below). Energy and efficiency calibration of the γ-ray spectra were performed with ^{182}Ta, ^{152}Eu, and ^{56}Co sources. The precisely known energies of the $4^+ \rightarrow 2^+ \rightarrow 0^+$ cascade in the strong ^{60}Ni+4p channel provided an additional "in beam" bench mark. The γ-ray energy range was set to 0.1-6 MeV.

Protons and α particles were identified in the MICROBALL on the basis of two independent pulse-shape discrimination techniques [13]. For this experiment, both the inverse kinematics and restrictive particle gating (aiming at the most effective channel selection, cf. [2]) resulted in a proton detection *and* identification efficiency of nearly 80 % while that of α particles amounted to some 65 %. Neutrons and γ rays were very well discrimated by the combination of pulse-shape analysis of the neutron detector signals and time-of-flight measurements relative to the RF-frequency of the cyclotron. The energies of the charged particles detected in the MICROBALL were used to evaluate the momenta of the individual recoiling nuclei. This "kinematic correction" results in a more precise Doppler-shift correction of the γ-ray energies and significantly improves their energy resolution, especially in these light systems.

The events were sorted off-line into various E_γ projections, E_γ-E_γ matrices, and E_γ-E_γ-E_γ cubes subject to appropriate evaporated particle and analysis conditions. Careful successive subtractions of contaminations from higher fold charged-particle channels, which may leak through when one or more proton or α escaped detection or identification, resulted in purified singles projections, $\gamma\gamma$ matrices, and γ-gated spectra for a given isotope. Based on the yields of (known) ground-state transitions, corrected for γ- and particle detection efficiency, experimental relative cross sections were deduced. The numbers relevant to the nuclei discussed in this paper are given in Table 1. Altogether some 25 nuclei were produced with measurable cross section. Among them, the strongest channel, ^{58}Ni+1α2p, comprises nearly 1/3 of the total fusion cross section. In contrast, ^{55}Ni+2α1n represents the weakest channel identified, with about 0.004 % relative cross section [2].

Coincidence, intensity balance, and summed energy relations were inspected to deduce the high-spin excitation schemes. The γ-ray energies and their relative yields presented in Tables 2–7 are based on the previously mentioned purified particle-gated singles projections. For weak transitions and/or doublet structures γ-gated spectra obtained from appropriately particle-gated $\gamma\gamma$ matrices were considered. The spectrum analysis was performed using the code ViewSpectra developed at the University of Cologne [14]. The deduction of the extensive excitation schemes of the (moderately strong) channels ^{54}Fe+2α2p, ^{55}Co+2α1p, and ^{57}Ni+1α2p1n required the use of the Radware-(cube)-analysis package [15].

In order to extract the multipolarities of the transitions *and* collect sufficient statistics, the 82 detectors of GAMMASPHERE were grouped into four "pseudo"-rings labelled "30", "53", "70", and "83": Ring "30" consists of the 15 detectors at 142.6°, 148.3°, and 162.7°. The cosines of these angles, mirrored to angles between 0° and 90° and weighted by the number of detectors, average to $\overline{\theta} = 30°$. Ring "53" ($\overline{\theta} = 53°$) comprised 28 detectors (50.1°, 58.3°, 121.7°, and 129.9°), ring "70" ($\overline{\theta} = 70°$) 14 detectors (69.8° and 110.2°), and ring "83" ($\overline{\theta} = 83°$) 25 detectors (79.2°, 80.7°, 90.0°, 99.3°, and 100.8°). Particle-gated (and purified) singles projections were created for these four rings of detectors, as well as $\gamma\gamma$ matrices with one γ ray originating from one distinct ring while the second could come from any detector. Sums of γ-gated spectra (projected on the respective ring) as well as the purified singles projections formed the basis for the angular distribution analysis. If applicable, a Legendre least-squares fit was performed over the four data points to deduce the (normalized) angular distribution coefficients a_2 and a_4 of the angular distribution formula [16]

$$W(\theta) = 1 + q_2 a_2 P_2(cos\theta) + q_4 a_4 P_4(cos\theta). \qquad (1)$$

Table 1. Some experimental relative cross-sections for the reaction ^{36}Ar +^{28}Si at $\overline{E}_{\rm beam}$ = 136 MeV deduced from the yields of known ground-state and bandhead transitions in various particle-gated spectra

reaction channel	$\sigma_{\rm rel}$ (%)	reaction channel	$\sigma_{\rm rel}$ (%)
^{54}Fe+2α2p	1.0(2)	^{56}Ni+2α	0.020(3)
^{54}Co+2αpn	0.12(3)	^{57}Ni+α2pn	3.8(8)
^{55}Co+2αp	2.0(2)	^{58}Cu+αpn	0.30(7)

Table 2. The energies of excited states in ^{54}Fe, the transitions energies and relative intensities of the γ rays placed in the level scheme, angular distribution ratios, the DCO-ratios of three different angle combinations, the deduced mixing ratios, and the spins and parities of the initial and final states of the γ rays

E_x (keV)	E_γ (keV)	I_{rel} (%)	R_{30-83}	R_{DCO} 30°-53°	30°-83°	53°-83°	α_2 [a]	$\delta(E2/M1)$	Mult. Ass.	I_i^π ($\hbar$)	I_f^π ($\hbar$)
1407.8(2)	1407.8(2)	100(3)	1.24(6)[b]	1.02(4)	1.02(5)	0.98(5)			$E2$	2^{+c}	0^+
2537.4(2)	1129.6(1)	98(3)	1.21(6)[b]	1.01(5)	1.02(5)	0.99(5)			$E2$	4^{+c}	2^+
2948.6(2)	411.2(1)	72(2)	1.00(4)[b]	0.96(5)	0.95(5)	1.07(6)			$E2$	6^{+c}	4^+
3294.2(4)	756.8(4)	12(1)	0.92(4)	1.03(8)	1.07(10)	1.01(8)	0.62	$-1.2 < \delta < -0.05$	$(\Delta I = 0)$	4^{+c}	4^+
	1887(1)	3.5(2)								4^+	2^+
3344.2(4)	806.9(4)	1.0(2)	0.63(8)	0.53(18)	0.79(44)	1.07(32)			$(E2/M1)$	3^{+c}	4^+
	1937(2)	1.0(2)								3^+	2^+
4030.9(4)	736.8(4)	7.5(5)	0.43(3)	0.69(8)	0.49(6)	0.76(6)	0.63	$+0.14(^{10}_{7})$	$E2/M1$	5^+	4^+
	1494(1)	1.5(3)								5^+	4^+
4047.4(6)	703.6(6)	1.2(2)	0.47(7)						$(E2/M1)$	4^{+c}	3^+
	2640(2)	1.0(2)								4^+	2^+
4655.2(7)	608(1)	0.3(1)								5^+	4^+
	1361(1)	2.5(5)	0.52(5)	0.85(24)	0.63(17)	0.68(13)			$E2/M1$	5^+	4^+
5045.4(3)	1015.0(5)	0.9(2)		0.44(20)	0.67(21)	0.73(17)			$(E2/M1)$	6^{+c}	5^+
	2097(1)	4.4(6)	1.26(8)	1.17(13)	1.13(15)	0.95(12)	0.65	~ -1.0	$(\Delta I = 0)$	6^+	6^+
5280.1(7)	625.0(6)	0.4(1)	0.82(16)							6^+	5^+
	1249(1)	1.4(3)	0.52(4)[d]	0.47(12)	0.62(15)	0.68(12)			$E2/M1$	6^+	5^+
	1986(2)	1.6(4)	[d]							6^+	4^+
	2332(2)	0.6(2)								6^+	6^+
5481.8(7)	1435(1)	0.3(1)								(5^+)	4^+
	2944(1)	2.6(4)	1.10(10)	1.01(25)	0.73(19)	1.14(23)	0.66	~ -0.3	$(E2/M1)$	(5^+)	4^+
5927.2(2)	881.9(3)	2.2(3)	0.51(4)	0.77(12)	0.56(9)	0.73(8)	0.67	$+0.07(^{11}_{8})$	$E2/M1$	7^+	6^+
	1895(1)	0.5(2)								7^+	5^+
	2979(1)	11(1)	1.49(9)	1.35(11)	1.31(14)	0.97(11)	0.67	~ -1.0	$E2/M1$	7^+	6^+
6297(1)	3348(2)	2.7(3)		$\gg 1$	$\gg 1$	~ 1				(7^+)	6^+
6380.0(2)	3431.2(5)	29(1) [e]	1.26(6)	1.00(10)	1.01(11)	0.99(10)			$E2$	8^{+c}	6^+
6526.0(2)	145.9(2)	27(1) [e]		0.96(8)	1.05(11)	1.21(12)			$E2$	10^{+c}	8^+
	3578(2)	0.5(1)[e]							$E4$	10^+	6^+
6551(1)	1069(1)	0.2(1)									(5^+)
	3602(2)	0.5(2)									6^+
6723.4(2)	197.4(2)	18(1)	0.42(2)	0.85(14)	0.60(11)	0.67(11)	0.68	-0.07(6)	$E2/M1$	9^+	10^+
	796.4(2)	5.0(3)	1.20(8)	1.10(10)	1.11(12)	1.01(10)			$E2$	9^+	7^+
6864.1(4)	936.9(5)	3.6(4)	0.61(3)	0.97(13)	0.71(9)	0.84(8)	0.69	-0.09(12)	$E2/M1$	8^+	7^+
	1819(1)	0.8(2)								8^+	6^+
	3915(2)	3.0(3)	1.21(7)	0.97(16)	1.21(21)	1.06(15)			$(E2)$	8^+	6^+
7075(2)	778(1)	0.4(2)									(7^+)
	1148(1)	0.3(1)									7^+
	4126(3)	0.9(2)									6^+
7351.3(4)	487.2(2)	4.2(5)	0.55(4)	0.79(8)	0.53(6)	0.85(6)	0.70	-0.01(7)	$E2/M1$	9^+	8^+
	971.6(6)	1.0(3)								9^+	8^+
	1423.8(6)	2.8(4)	1.39(10)	1.03(16)	1.06(18)	1.22(22)			$(E2)$	9^+	7^+
7503.4(3)	780.0(2)	16(1)	0.67(3)	0.78(9)	0.69(8)	0.92(8)	0.70	+0.06(6)	$E2/M1$	10^+	9^+
				1.00(7)[f]	1.10(8)[f]	0.89(5)[f]					
	978(1)	2.4(3)								10^+	10^+
7566(2)	4617(3)	0.8(2)									6^+
8018.6(3)	1492.4(4)	21(1)	0.82(5)	0.75(14)	0.72(24)	0.70(17)	0.71	$-0.02(^{14}_{12})$	$E2/M1$	11^+	10^+
				0.81(10)[f]	0.82(11)[f]	0.94(9)[f]					
8319(1)	753(1)	0.5(2)									
	1769(2)	0.2(1)									
	2022(1)	0.2(1)									(7^+)
8374(1)	1994(1)	2.0(5)	1.12(7)	0.94(15)	1.27(22)	0.85(12)			$(E2)$	(10^+)	8^+
8577.6(5)	559(1)	0.4(1)								(10^+)	11^+
	1226.2(5)	2.1(3)	0.69(5)	1.27(33)	0.76(22)	0.97(20)			$(E2/M1)$	(10^+)	9^+

Table 2. Continued

E_x (keV)	E_γ (keV)	I_{rel} (%)	R_{30-83}	R_{DCO} 30°-53°	R_{DCO} 30°-83°	R_{DCO} 53°-83°	α_2[a]	$\delta(E2/M1)$	Mult. Ass.	I_i^π ($\hbar$)	I_f^π ($\hbar$)
8807.8(3)	788.8(6)	0.6(1)								11^+	11^+
	1304.5(4)	7.0(9)	0.74(5)	0.75(21)	0.76(16)	0.82(13)	0.73	$+0.03(^{11}_{7})$	$E2/M1$	11^+	10^+
	2282(2)	5(1)								11^+	10^+
9123(1)	1772(1)	0.8(2)									9^+
9845.0(4)	1037.2(4)	4.1(8)	0.75(6)	0.88(20)[f]	0.90(25)[f]	0.95(16)[f]			$E2/M1$	12^+	11^+
	1826.4(7)	18(1)	0.87(4)	1.02(13)[f]	1.08(16)[f]	0.95(10)[f]			$E2/M1$	12^+	11^+
	2342(2)	0.4(1)								12^+	10^+
	3319(2)	10(1)	1.18(11)							12^+	10^+
9995(1)	2492(2)	0.3(1)									10^+
	3270(3)	0.3(1)									9^+
10130.7(7)	1323(1)	2.2(3)	1.05(7)[d]							(12^+)	11^+
	2112(1)	1.0(2)	1.49(22)							(12^+)	11^+
10541.7(6)	1734(1)	0.8(2)								(11)	11^+
	1964(1)	0.3(1)								(11)	(10^+)
	2523(2)	0.4(1)								(11)	11^+
	3037(2)	0.4(1)								(11)	10^+
	4016(1)	1.2(2)								(11)	10^+
11093.1(5)	1248.1(3)	32(1)	0.94(5)[d]	1.23(22) [f]	1.15(24)[f]	0.88(20)[f]			$E2/M1$	13^+	12^+
	3074(2)	2.8(3)								13^+	11^+
11113.2(7)	571.5(4)	2.8(2)	0.54(4)						$E2/M1$	(12)	(11)
	1118(1)	0.3(1)								(12)	
	2306(2)	1.5(3)	0.74(6)						$(\Delta I = 1)$	(12)	11^+
	3095(3)	0.9(2)								(12)	11^+
12042.6(8)	929.4(4)	4.5(4)	0.79(9)						$(E2/M1)$	(13)	(12)
12313.8(6)	1220.7(4)	13(1)	0.89(4)	0.98(13)[f]	1.01(15)[f]	1.09(13)[f]			$E2/M1$	14^+	13^+
	2183(2)	0.2(1)								14^+	(12^+)
12953(1)	1860(1)	2.2(4)	0.81(9)						$(E2/M1)$	(14^+)	13^+
13358(1)	1315(1)	1.8(3)	[d]								
14388(1)	1435(1)	0.2(1)									(14^+)
	2074(2)	2.5(5)	1.41(10)								14^+
15062(2)	1704(2)	0.3(1)									

[a] The attenuation coefficients were fixed using the relation $\alpha_2 = 0.55 + 0.02 \cdot E_x(\mathrm{MeV})$ and uncertainties $\Delta\alpha_2 \pm 0.05$
[b] Value taken from the backed-target experiment to avoid distortions from the effect of deorientation at low spins
[c] Assignment (also) based on [25]
[d] Doublet structure
[e] Intensities taken from the backed-target experiment. The 6526 keV 10^+ level is an isomer with $T_{1/2} = 364(7)$ ns
[f] R_{DCO} deduced from spectra gated with the 197 and 1248 keV transitions (stretched $\Delta I = 1$)

P_2 and P_4 denote the Legendre polynomials while q_2 and q_4 account for the attenuation due to the finite opening angles of the Ge detectors [17]. However, the limited amount of statistics and, hence, too large error margins for most of the present transitions and/or the lack of a data points near zero degrees prevented a detailed analysis, i.e., a proper determination of the width of the presumed Gaussian distribution of the magnetic substates (alignment σ) or mixing ratios $\delta(E2/M1)$ for $\Delta I \leq 1$ transitions. Instead, the most sensitive ratio of yields of ring "30" and ring "83", R_{30-83}, is given in Tables 2–7 and shown in Fig. 1 as a function of excitation energy. The ratios from the fairly strong channels ^{54}Fe, ^{55}Co, and ^{57}Ni are plotted in case the multipolarities could be assigned or at least suggested. Filled symbols represent stretched $\Delta I = 2$ (mainly $E2$) transitions, open symbols stretched $\Delta I = 1$ (mainly mixed $E2/M1$) transitions. A few $\Delta I = 0$ transitions are denoted with a cross. The $\Delta I = 2$ transitions are located around $R_{30-83} \approx 1.2$ with slightly increasing values for higher excitation energies, i.e., a more pronounced alignment width σ. The values for the vast majority of the $\Delta I = 1$ transitions is less than one, i.e., distinctly different from the $\Delta I = 2$ mean. However, a number of $\Delta I = 1$ transitions were found to have a considerable $E2$ admixture which gives rise to ambiguities if one were to assign spins (and parities) *only* based on this ratio. Therefore, the ratio is used to *suggest* or *support* multipolarity assignments which were fixed via multiple directional correlations of oriented states (DCO-ratios). Here, these are defined as

$$R_{DCO}(\text{30-83};\gamma_1,\gamma_2) = \frac{I(\gamma_1 \text{ at } 30°;\ \text{gated with } \gamma_2 \text{ at } 83°)}{I(\gamma_1 \text{ at } 83°;\ \text{gated with } \gamma_2 \text{ at } 30°)}. \quad (2)$$

Table 3. The energies of excited states in ^{54}Co, the transitions energies and relative intensities of the γ rays placed in the level scheme, angular distribution ratios, and the spins and parities of the initial and final states of the γ rays

E_x (keV)	E_γ (keV)	I_{rel} (%)	R_{30-83}	I_i^π ($\hbar$)	I_f^π ($\hbar$)
936.8(4)	936.8(4)	76(7)	0.94(9)	1^{+a}	0^+
1445.1(5)	508.3(3)	52(5)	0.60(8)	2^{+a}	1^+
1820.6(5)	375.5(2)	35(4)	0.78(10)	$(3^+)^a$	2^+
1887(2)	1688(2)	11(2)		$(5^+)^a$	$(7)^{+a}$
2651.2(7)	764(2)	4(2)		$(4^+)^a$	(5^+)
	830.5(5)	25(3)	0.86(12)	(4^+)	(3^+)
2910.9(7)	259.6(3)	8(1)		$(6^+)^a$	(4^+)
	1025(2)	2(1)		(6^+)	(5^+)
3173(2)	2974(1)	100(5)	1.16(14)	(9^+)	$(7)^+$
4729(3)	1557(1)	53(6)	> 1	(11^+)	(9^+)
5048(4)	1875(3)	5(1)			(9^+)
7243(4)	2514(3)	9(2)			(11^+)

[a] Assignment based on [25]

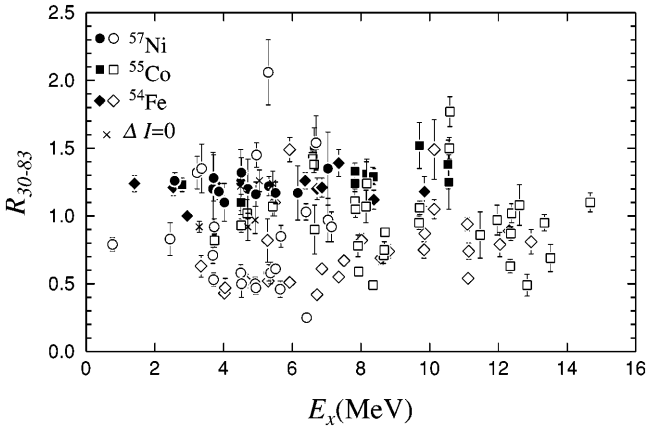

Fig. 1. Ratios R_{30-83} of yields of transitions in ^{54}Fe (rhombus), ^{55}Co (squares), and ^{57}Ni (circles) detected at mean detector angles of 30° and 83° degrees, respectively. See text for details

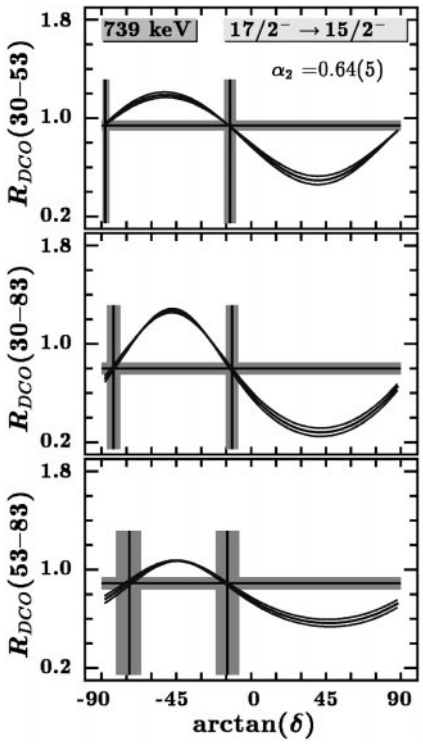

Fig. 2. The analysis of DCO-ratios of different detector angle combinations for the 739 keV $17/2^- \rightarrow 15/2^-$ transition in ^{55}Co is presented to deduce its multipole mixing ratio $\delta(E2/M1)$. The experimental DCO ratio (horizontal line) is plotted with its error margin indicated in grey. The DCO-ratio calculated for the given alignment (and error margins) and depending on the mixing ratio δ is shown by the three curves. The crossing(s) of the curve with the experimental DCO-ratio mark possible solutions for the mixing ratio, indicated by the vertical solid lines. Again, the shaded area provides the error margins

The DCO-ratios R_{DCO}(30-53) and R_{DCO}(53-83), invoking pseudo ring "53", are defined accordingly. The DCO-ratios were corrected for the different detection efficiencies at different detection angles. In general, known stretched $E2$ transitions are used for gating. Then one expects $R_{DCO} = 1.0$ for observed stretched $E2$ transitions for *all* three combinations [18,19]. Contrary, DCO-ratios of stretched $\Delta I = 1$ or $\Delta I = 0$ transitions depend on both the ring combination *and* the possible $\delta(E2/M1)$ mixing ratio. In fact, the common ambiguity between a possible solution having a small ($\delta(E2/M1) \approx 0$) or a large ($|\delta(E2/M1)| \gg 0$) mixing ratio can be surpassed [19]. This is illustrated in Fig. 2 providing the analysis for the 739 keV $17/2^- \rightarrow 15/2^-$ transition in ^{55}Co. The experimental DCO ratio (horizontal line) is plotted with its error margin indicated in grey. The theoretical DCO-ratio (for a given alignment width and error margin) was calculated depending on the mixing ratio δ and represented by the three curves. The crossing(s) of the curve with the experimental DCO-ratio mark possible solutions for the mixing ratio, indicated by the vertical solid lines. Again, the shaded area provides the error margin(s). In the case of the 739 keV transition in ^{55}Co only the three solutions near $\arctan(\delta) \approx 12°$ overlap while those at large negative values can be excluded. Here, the weighted mean yields $\delta(E2/M1) = -0.22(4)$, the number given in Table 4.

The alignment coefficient $\alpha_2 = a_2/A_{2,\max}$ was calculated using the relation $\alpha_2 = 0.55 + 0.02 \cdot E_x(\text{MeV})$ and uncertainties $\Delta\alpha_2 \pm 0.05$. This assumption provides a reasonable estimate of the alignment as long as no nanosecond isomer is encountered in the course of the decay sequence [20]. Candidates for stretched, parity changing $E1$ transitions shall have a mixing ratio consistent with zero. The DCO-ratios given in Tables II-VII represent mean values of different (γ-)gating conditions and, if applicable, data from both the unbacked and backed target experiments. The mixing ratios are mean values for different ring combinations and from the analysis of both DCO-ratios (cf. Fig. 2) and gated angular distributions. The multipolarity and, hence, spin and parity assignments are also

Table 4. The energies of excited states in ^{55}Co, the transitions energies and relative intensities of the γ rays placed in the level scheme, angular distribution ratios, the DCO-ratios of three different angle combinations, the deduced mixing ratios, and the spins and parities of the initial and final states of the γ rays

E_x (keV)	E_γ (keV)	I_{rel} (%)	R_{30-83}	R_{DCO} 30°-53°	30°-83°	53°-83°	α_2 [a]	$\delta(E2/M1)$	Mult. Ass.	I_i^π ($\hbar$)	I_f^π ($\hbar$)
2973.4(2)	2973.4(2)	100(3)	1.23(5)	1.01(5)	1.03(5)	0.98(5)			$E2$	$11/2^-$	$7/2^-$
3736.5(2)	763.2(1)	11(1)	0.82(5)	0.65(9)	0.60(13)	0.80(11)	0.62	+0.01(8)	$E2/M1$	$13/2^-$	$11/2^-$
3774.4(2)	37.9(3) [b]	5.5(5)								$15/2^-$	$13/2^-$
	801.0(1)	79(2)	1.22(6)	0.98(4)	0.97(4)	1.01(5)			$E2$	$15/2^-$	$11/2^-$
4513.7(2)	739.0(1)	73(2)	0.93(5)	0.94(4)	0.80(5)	0.89(5)	0.64	-0.22(4)	$E2/M1$	$17/2^-$	$15/2^-$
	777.9(2)	5.2(2)	1.10(6)	0.93(11)	1.11(16)	0.98(10)			$E2$	$17/2^-$	$13/2^-$
4686.2(4)	949.6(3)	1.7(2)	1.02(10)		0.68(36)					$15/2^-$ [c]	$13/2^-$
	1713(1)	1.8(3)								$15/2^-$	$11/2^-$
4920.7(4)	1146.1(4)	1.2(1)	0.97(10)	1.12(22)	1.15(26)	1.18(20)			$(\Delta I = 0)$	$(15/2^-)$	$15/2^-$
5431.6(3)	745.2(6)	0.7(2)								$17/2^-$	$15/2^-$
	917.8(5)	1.0(2)	1.24(9)		0.85(20)				$(\Delta I = 0)$	$17/2^-$	$17/2^-$
	1657.2(4)	6.8(2)	1.07(7)	1.02(9)	0.89(9)	0.92(8)	0.66	-0.31(7)	$E2/M1$	$17/2^-$	$15/2^-$
6332.4(5)	900.6(8)	0.3(1)								$(17/2^-)$	$17/2^-$
	1412(1)	0.2(1)								$(17/2^-)$	$(15/2^-)$
	1646(1)	0.1(1)								$(17/2^-)$	$15/2^-$
	1819(1)	1.2(2)	[d]	0.96(14)	0.98(14)	0.88(14)			$(\Delta I = 0)$	$(17/2^-)$	$17/2^-$
6596.4(3)	1675(1)	0.1(1)								$19/2^-$	$(15/2^-)$
	2082.7(3)	25(1)	1.42(6)	1.08(7)	1.22(10)	1.01(7)	0.68	-0.5(2)	$E2/M1$	$19/2^-$	$17/2^-$
	2822(1)	8.5(3)	1.44(8)	0.91(8)	0.99(10)	1.03(9)			$E2$	$19/2^-$	$15/2^-$
6641.4(3)	1208(1)	0.3(1)	0.90(18)							$19/2^-$	$17/2^-$
	2127.6(3)	20(1)	1.38(6)	1.11(7)	1.21(8)	1.07(6)	0.68	-0.6($\frac{1}{2}$)	$E2/M1$	$19/2^-$	$17/2^-$
	2868(1)	3.6(2)	1.52(13)	1.14(15)	1.18(25)	1.02(13)			$E2$	$19/2^-$	$15/2^-$
7529.2(5)	2843(2)	0.6(1)								$19/2^-$ [c]	$15/2^-$
	3015(1)	0.8(1)	1.43(20)							$19/2^-$	$17/2^-$
7833.0(3)	1191.6(4)	0.8(2)	1.11(9)							$21/2^-$	$19/2^-$
	1236.1(4)	1.8(1)	1.05(6)	1.05(14)	1.23(19)	0.90(11)	0.71	-0.4(2)	$(E2/M1)$	$21/2^-$	$19/2^-$
	2402(1)	1.6(1)	1.24(6)							$21/2^-$	$17/2^-$
	3319.3(3)	20(1)	1.33(6)	0.98(6)	1.06(7)	1.00(6)			$E2$	$21/2^-$	$17/2^-$
7855(2)	3169(2)	0.2(1)									$15/2^-$
7920.5(5)	1324(1)	0.2(1)								$19/2^-$	$19/2^-$
	1588(1)	0.7(1)	0.78(8)							$19/2^-$	$(17/2^-)$
	3407.9(7)	6.5(3)	0.59(3)	0.71(8)	0.47(6)	0.72(6)	0.71	+0.12(7)	$E2/M1$	$19/2^-$	$17/2^-$
8090(2)	2658(2)	0.3(1)									$17/2^-$
	3169(2)	0.4(2)									$(15/2^-)$
	3577(3)	0.3(2)									$17/2^-$
8158.5(4)	1516.7(6)	0.6(1)	1.07(12)							$21/2^-$ [c]	$19/2^-$
	1562.1(6)	1.3(1)	1.24(18)							$21/2^-$	$19/2^-$
	2728(1)	1.9(3)	1.42(28) [d]							$21/2^-$	$17/2^-$
	3645(2)	1.6(2)	1.31(9)		1.23(30)			[d]		$21/2^-$	$17/2^-$
8348.7(3)	515.5(2)	5.0(2)	0.49(3)	0.79(7)	0.37(5)	0.53(7)	0.72	[e]	$E2/M1$	$23/2^-$	$21/2^-$
	1707.2(4)	16(1)	1.30(6)	1.01(6)	1.10(6)	1.06(6)			$E2$	$23/2^-$	$19/2^-$
	1752.4(3)	13(1)	1.29(6)	1.04(6)	1.04(6)	1.05(6)			$E2$	$23/2^-$	$19/2^-$
8400.6(8)	1804(1)	1.0(2)									$19/2^-$
	3887(2)	0.8(1)									$17/2^-$
8686.9(5)	766.4(3)	5.2(2)	0.71(6)	1.20(22)	0.75(17)	0.79(16)	0.72	-0.1(2)	$\Delta I = 1$	21/2	$19/2^-$
	2091(2)	0.8(2)	1.17(8) [d]	1.10(19)	0.93(18)	0.92(14)		[d]		21/2	$19/2^-$
8689.5(3)	340.5(2)	0.6(1)	0.75(6)		0.47(16)				$E2/M1$	$23/2^-$	$21/2^-$
	856.6(2)	11(1)	0.88(4)	0.94(6)	0.89(6)	0.93(5)	0.72	-0.25(6)	$E2/M1$	$23/2^-$	$21/2^-$
	1160.2(5)	0.4(1)								$23/2^-$	$19/2^-$
	2095(1)	5.2(4)	1.17(8) [d]	1.10(19)	0.93(18)	0.92(14)		[d]		$23/2^-$	$19/2^-$
9698.5(3)	1008.7(3)	3.5(1)	0.95(5)	0.93(9)	0.75(9)	0.86(8)	0.74	-0.19(8)	$E2/M1$	$25/2^-$	$23/2^-$
	1349.9(2)	17(1)	1.06(5)	1.03(6)	0.96(6)	0.97(5)	0.74	-0.35(7)	$E2/M1$	$25/2^-$	$23/2^-$
	1539.9(6)	0.8(1)	1.52(17)							$25/2^-$	$21/2^-$
	1865.8(8)	2.0(1)	1.30(10) [d]	1.11(23)	1.00(14)	0.96(22)			$E2$	$25/2^-$	$21/2^-$

Table 4. Continued

E_x (keV)	E_γ (keV)	I_{rel} (%)	R_{30-83}	R_{DCO} 30°-53°	30°-83°	53°-83°	$\alpha_2{}^a$	$\delta(E2/M1)$	Mult. Ass.	I_i^π ($\hbar$)	I_f^π ($\hbar$)
9782.1(9)	1433(1)	0.5(1)	0.94(13)								$23/2^-$
	3187(2)	0.6(1)	1.56(25)								$19/2^-$
10112.8(7)	1426.0(5)	2.5(1)	1.43(9)	1.01(12)	1.21(17)	1.03(12)			$(E2/M1)$	(23/2)	21/2
	1712(1)	0.3(1)								(23/2)	
10545.4(5)	1859(1)	0.8(2)	1.30(10)[d]							(23/2)[c]	21/2
	2626(1)	1.1(1)	1.38(18)							(23/2)	$19/2^-$
	2714(2)	1.0(2)	1.25(20)							(23/2)	$21/2^-$
10579.8(5)	880(1)	0.3(1)								$25/2^-$	$25/2^-$
	1889.5(6)	3.0(2)	1.50(8)	1.12(13)	1.11(11)	1.25(14)	0.76	-0.6(2)	$E2/M1$	$25/2^-$	$23/2^-$
	2231(1)	2.9(3)	1.77(11)	1.30(20)	1.26(16)	1.15(20)	0.76	$-1.2(^{7}_{10})$	$E2/M1$	$25/2^-$	$23/2^-$
10760(1)	2411(2)	0.5(1)									$23/2^-$
	2927(2)	1.0(2)									$21/2^-$
11469.9(5)	924.7(3)	0.7(2)	0.86(7)		0.62(19)				$(\Delta I = 1)$	25/2	(23/2)
	2781(2)	1.5(5)	1.95(13)[d]	1.11(14)	1.26(22)	1.11(14)		[d]		25/2	$23/2^-$
	2783(2)	2.4(3)	1.95(13)[d]	1.11(14)	1.26(22)	1.11(14)		[d]		25/2	21/2
	3640(2)	0.6(2)			1.23(30)			[d]		25/2	$21/2^-$
11908.0(5)	1363(1)	0.2(1)	1.45(11)[d]					[d]		25/2	(23/2)
	3222(2)	0.3(1)	1.10(16)							25/2	21/2
	3560(2)	0.2(1)								25/2	$23/2^-$
	4075(3)	0.3(1)								25/2	$21/2^-$
11962.6(8)	2264(1)	2.0(2)	2.2(5)[d]		1.20(20)			[d]		(27/2)	$25/2^-$
	3274(2)	1.8(1)	1.45(10)							(27/2)	$23/2^-$
	3615(2)	0.9(2)	0.97(11)							(27/2)	$23/2^-$
12118.5(8)	1359(1)	0.8(2)	1.45(11)[d]					[d]			
	2420(1)	2.0(2)									$25/2^-$
12363.0(5)	455.0(1)	0.5(1)	0.63(5)		0.56(12)				$\Delta I = 1$	27/2	25/2
	893.2(2)	2.3(1)	0.87(5)	0.94(11)	0.85(12)	0.92(10)	0.80	-0.24(10)	$E2/M1$	27/2	25/2
	1782.9(3)	2.0(1)	1.02(7)	0.73(13)	0.67(11)	0.86(13)	0.80	-0.1(2)	$\Delta I = 1$	27/2	$25/2^-$
	1818(1)	1.0(2)	1.49(13)[d]	0.96(14)	0.98(14)	0.88(14)		[d]		27/2	(23/2)
	4013(3)	0.4(1)								27/2	$23/2^-$
12613(1)	2915(3)	0.4(1)									$25/2^-$
	3925(3)	0.6(1)									$23/2^-$
	4263(3)	0.6(2)									$23/2^-$
12835(1)	2255(2)	1.0(1)	1.53(51)							(27/2)[c]	$25/2^-$
	2722(1)	0.7(2)	1.42(28)[d]							(27/2)	(23/2)
	3138(2)	0.8(1)	0.49(8)						$(\Delta I = 1)$	(27/2)	$25/2^-$
13163(1)	4812(2)	0.7(2)									$23/2^-$
13339.1(5)	976.1(2)	3.3(1)	0.95(6)	0.85(9)	1.00(12)	0.82(8)	0.82	-0.2(1)	$E2/M1$	29/2	27/2
13516.4(8)	1398(1)	0.5(2)	0.69(10)						$(E2/M1)$	$(27/2^-)$	$(25/2^-)$
	2936(3)	0.5(1)								$(27/2^-)$	$25/2^-$
	3818(1)	1.7(1)	1.32(10)		0.65(17)				$(E2/M1)$	$(27/2^-)$	$25/2^-$
13685(3)	5336(3)	0.2(1)									$23/2^-$
13818(1)	1856(1)	0.7(1)									(27/2)
	4119(2)	1.2(1)									$25/2^-$
14125(3)	4426(3)	1.0(2)									$25/2^-$
14672.3(6)	1333.2(3)	2.1(2)	1.10(7)	1.28(19)	1.00(16)	0.79(11)	0.84	$\sim -0.3; \sim -3.0$	$E2/M1$	31/2	29/2
	1837(1)	0.3(1)								31/2	(27/2)
14730(3)	5031(3)	0.1(1)									$25/2^-$
14881(1)	1063(1)	0.3(1)									
	1365(1)	0.2(1)	1.45(11)[d]					[d]			$(27/2^-)$
	1718(1)	0.2(1)									
	2268(2)	0.7(2)	2.2(5)[d]		1.20(20)			[d]			
	2919(2)	0.5(1)									(27/2)

[a] The attenuation coefficients were fixed using the relation $\alpha_2 = 0.55 + 0.02 \cdot E_x(\mathrm{MeV})$ and uncertainties $\Delta\alpha_2 \pm 0.05$
[b] Existence and yield deduced from coincidence relation between the 763 and 739 keV transitions
[c] The spin and parity assignment of this intermediate level is based on a known spin difference of four (six) between the initial and final states of a γ-ray cascade consisting of two (three) transitions assuming that only transitions with $\Delta I \leq 2$ are observed
[d] Doublet structure
[e] No consistent solution

Table 5. The energies of excited states in ^{56}Ni, the transitions energies and relative intensities of the γ rays placed in the level scheme, angular distribution and the DCO-ratios, and the spins and parities of the initial and final states of the γ rays

E_x (keV)	E_γ (keV)	I_{rel} (%)	R_{30-83}	R_{DCO} 30°-83°	I_i^π ($\hbar$)	I_f^π ($\hbar$)
2701(1)	2701(1)	100(3)	1.42(13)	0.95(28)	2^{+a}	0^+
3925(1)	1224(1)	95(3)	1.24(10)	1.01(17)	4^{+a}	2^+
5317(1)	1392(1)	80(3)	1.50(21)	0.89(16)	6^{+a}	4^+
5351(1)	2650(2)	8(1)			2^{+a}	2^+
	5351(3)	5(1)			2^+	0^+
6327(1)	976(1)	10(1)	1.49(18)		(4^+)	2^+
	2402(2)	6(2)	1.44(39)		(4^+)	4^+
	3626(2)	15(1)	1.51(32)		(4^+)	2^+
7653(2)	1326(1)	28(2)	1.27(15)		(6^+)	(4^+)
	3727(3)	2(1)			(6^+)	4^+
7956(2)	2639(2)	45(2)	1.26(13)	1.16(30)	8^+	6^+
8225(2)	2908(2)	10(1)	1.14(23)		(8^+)	6^+
9310(2)	1657(1)	25(1)	1.15(15)		(8^+)	(6^+)
9419(3)	1463(1)	30(2)	1.30(14)	0.88(24)	10^+	8^+
9736(3)	846(1)	2(1)				
	2083(2)	2(1)				6^+
10679(2)	2454(2)	6(1)			$(10^+)^c$	(8^+)
10937(2)	1201(1)	7(1)			(9)	
	1627(1)	13(1)	0.90(13)		(9)	(8^+)
11297(3)	1987(2)	10(1)	1.30(36)		(10^+)	(8^+)
12360(3)	1681(2)	2(1)			(12^+)	(10^+)
	2941(3)	15(1)	1.67(28)	1.02(40)	(12^+)	10^+
12509(3)	1572(1)	18(2)	1.31(18)		(11)	(9)
13580(4)	2283(2)	6(1)			$(12^+)^b$	(10^+)
14454(4)	1945(2)	13(1)	1.24(18)		(13)	(11)
14737(5)	2377(2)	10(1)	1.46(21)		(14^+)	(12^+)
16772(5)	2318(2)	10(1)			$(15)^b$	(13)
19520(7)	2748(3)	4(1)			$(17)^b$	(15)

[a] Assignment also based on [1]
[b] Assignment suggested by rotational band structure
[c] The spin and parity assignment of this intermediate level is based on a known spin difference of four between the initial and final states of a γ-ray cascade consisting of two transitions assuming that only transitions with $\Delta I \leq 2$ are observed

based on yrast arguments, i.e., the more intense a state is populated the higher its spin value with respect to excitation energy. In addition, stretched $\Delta I > 2$ transitions are generally excluded. The latter may lead to assignments of intermediate yrare levels if the spins (and parities) of the yrast levels were determined. They are labelled accordingly in the tables.

2.1 Experimental results for $^{54}_{26}$Fe$_{28}$

In a previous study, the high-spin yrast cascade of ^{54}Fe was followed up to the isomeric 6526 keV 10^+ level [21]. Additional γ-ray transitions of 197, 780, and 1492 keV were reported. The lifetime of $\tau = 525(10)$ ns allowed the measurement of the static magnetic dipole and electric quadrupole moment of the 10^+ state [22–24]. The study of light ion induced reactions provided a large number of low-spin states [25] of which we observed the levels at 3294, 3344, 4031, and 4047 keV. The only discrepancy found is the spin assignment of the 4031 keV level which clearly indicates $I = 5$ instead of $I = 4$ according to our angular distribution and correlation analysis of the 737 keV transition. Some 70 new transitions were placed in the proposed level scheme shown in Fig. 3a. It was extended up to an exitation energy of some 15 MeV and spins $I = 15$ or 16 $\hbar$. The latter value corresponds to the maximum possible spin of 2p-4h excitations within the fp shell. Table 2 provides the level energies, γ-ray energies and intensities, angular distribution and correlation ratios, and the spin and parity assignments.

Figure 4 provides γ-ray spectra for the ^{54}Fe+2α2p reaction channel. Panels (a) and (b) are sums of spectra in coincidence with the yrast $6^+ \rightarrow 4^+ \rightarrow 2^+ \rightarrow 0^+$ cascade requiring two alpha particles and two protons detected in MICROBALL and employing the backed (a) and unbacked (b) target data. Panel (a) clearly indicates the two bypasses of the 10^+ isomer, namely the 796-2979(=882+2097)-keV and the 487-3915(=937+2979)-keV sequences. Since these transitions do not show obvious Doppler broadening or Doppler shift, the corresponding 6723 keV 9^+ and 7351 keV 9_2^+ states must have lifetimes in excess of one picosecond. In contrast, the observed gamma decays [cf. Fig. 4b] of the higher lying levels are fast, i.e., even the accumulated lifetimes within a given sequence have to be significantly lower than one picosecond. Of specific interest is the 3578 keV transition seen in Fig. 4a: it was suggested [26] and now confirmed to mark a 1.9(4)% $10^+ \rightarrow 6^+$ $E4$ branch competing with the 146 keV $E2$ decay.

Numerous more transitions are visible in Fig. 4b. For example, the labelled 3348 and 3602 keV transitions form the basis of several yrare states shown on the left hand side of the level scheme in Fig. 3a. Most of these transitions were too weak to deduce spins or parities of the associated energy levels. Some of the new transitions are highlighted in Fig. 4c which is the spectrum in coincidence with the 197 keV $9^+ \rightarrow 10^+$ transition *above* the isomer. Next to several γ rays connecting the yrast and yrare high-spin part of the ^{54}Fe level scheme, peaks at 572 and 929 keV are present. The sum of spectra in coincidence with these two transitions is shown in Fig. 4d. They are found to form (together with the 1315 and tentative 1704 keV transitions) a regular band-like structure the decay of which is highly fragmented [cf. Fig. 3a]. The yields of the linking transitions, in particular the 4016 keV $(11) \rightarrow 10^+$ line, account for the full intensity observed for the band members. Though the average difference in γ-ray energies within the band (~ 370 keV) is typical for the superdeformed bands in the mass region [3,4,10] the R_{30-83} ratios for both the 572 and 929 keV transition clearly indicate stretched $\Delta I = 1$ character. The ratio of the 2306 keV line was used to suggest the spin $I = (12)$ for the 11113 keV level.

The yrast cascade above the isomer is formed by the four strong $\Delta I = 1$ transitions at 1492, 1826, 1248, and 1221 keV. The multipolarity assignments are based on

Table 6. The energies of excited states in ^{57}Ni, the transitions energies and relative intensities of the γ rays placed in the level scheme, angular distribution ratios, the DCO-ratios of three different angle combinations, the deduced mixing ratios, and the spins and parities of the initial and final states of the γ rays

E_x (keV)	E_γ (keV)	I_{rel} (%)	R_{30-83}	R_{DCO} 30°-53°	30°-83°	53°-83°	α_2[a]	$\delta(E2/M1)$ Ass.	Mult. ($\hbar$)	I_i^π ($\hbar$)	I_f^π
768.4(2)	768.3(2)	22(1)	0.79(5)				0.57	-0.15($^{11}_{8}$);$\geq$ 3	$E2/M1$	$5/2^{-}$[b]	$3/2^-$
2442.7(3)	1674(1)	0.6(2)								$5/2^{-}$[b]	$5/2^-$
	2443.0(6)	5.6(6)	0.83(12)						($E2/M1$)	$5/2^-$	$3/2^-$
2577.0(3)	1809(1)	1.6(5)								$7/2^-$	$5/2^-$
	2577.1(4)	100(3)	1.26(6)	1.03(6)	1.00(6)	0.97(5)			$E2$	$7/2^-$	$3/2^-$
3229.6(3)	2460.1(7)	4.8(3)	1.32(12)							$7/2^{-}$[b]	$5/2^-$
	3230(1)	2.5(2)								$7/2^-$	$3/2^-$
3361.8(3)	784(1)	1.0(5)								$7/2^{-}$[b]	$5/2^-$
	2593.4(7)	5.2(4)	1.35(18)							$7/2^-$	$5/2^-$
	3362(1)	0.8(2)								$7/2^-$	$3/2^-$
3701.1(4)	1124.0(3)	10(1)	0.71(6)	0.72(12)	0.70(12)	0.63(8)	0.62	-0.02($^{12}_{9}$)	$\Delta I = 1$	9/2	$7/2^-$
	2933(1)	2.0(4)	1.20(27)							9/2	$5/2^-$
3712.9(3)	483.1(2)	3.9(4)	0.53(5)						$E2/M1$	$9/2^-$	$7/2^-$
	1135.9(3)	14(1)	0.92(6)	0.79(10)	0.80(10)	1.05(11)	0.62	-0.15(9)	$E2/M1$	$9/2^-$	$7/2^-$
	1270.2(3)	5.7(3)	1.28(17)							$9/2^-$	$5/2^-$
3864.3(3)	151.3(2)	1.1(2)								$11/2^-$	$9/2^-$
	163.1(5)	0.3(1)								$11/2^-$	(9/2)
	1287.3(3)	74(2)	1.18(6)	0.94(6)	0.94(5)	1.00(5)			$E2$	$11/2^-$	$7/2^-$
4025.3(4)	3257(1)	4.1(5)	1.10(14)							$9/2^{-}$[c]	$5/2^-$
4185.4(3)	471.6(7)	0.6(1)								$9/2^{-}$[c]	$9/2^-$
	823.6(5)	0.9(2)								$9/2^-$	$7/2^-$
	957(1)	0.7(3)								$9/2^-$	$7/2^-$
	1608(1)	2.3(3)								$9/2^-$	$7/2^-$
	1744(1)	0.5(2)								$9/2^-$	$5/2^-$
	3417(1)	1.4(3)								$9/2^-$	$5/2^-$
4363(3)	3595(3)	0.4(1)									$5/2^-$
4501.0(3)	475.7(2)	1.6(2)	0.58(6)						$E2/M1$	$11/2^-$	$9/2^-$
	636.4(2)	4.6(3)	1.22(10)	1.15(13)	1.23(16)	1.03(11)	0.64	$\sim$ -0.5	$\Delta I = 0$	$11/2^-$	$11/2^-$
	788(1)	0.7(2)								$11/2^-$	$9/2^-$
	800.5(6)	1.0(2)	0.50(10)						$\Delta I = 1$	$11/2^-$	9/2
	1139.2(4)	4.2(6)	1.14(24)[d]							$11/2^-$	$7/2^-$
	1272(1)	0.8(3)								$11/2^-$	$7/2^-$
	1924(1)	4(1)	1.32(11)	1.01(13)	1.16(17)	1.14(15)		[d]	$E2$	$11/2^-$	$7/2^-$
4535(2)	3767(2)	0.8(2)									$5/2^-$
4710.0(3)	845.7(2)	4.3(6)	0.92(10)[d]	1.08(17)	0.95(17)	1.09(15)		[d]		$11/2^-$	$11/2^-$
	2133.2(7)	2.4(3)	1.20(22)	1.05(24)	1.15(28)	0.98(20)		[d]	($E2$)	$11/2^-$	$7/2^-$
4939.5(3)	229.5(2)	2.5(3)	0.50(5)	1.00(26)	0.70(21)	1.03(23)	0.65	-0.1(3)	$E2/M1$	$13/2^-$	$11/2^-$
	438.1(2)	5.2(3)	0.47(5)	0.55(16)	0.59(14)	0.80(16)	0.65	+0.1(2)	$E2/M1$	$13/2^-$	$11/2^-$
	754.1(2)	3.9(3)	0.88(20)[d]							$13/2^-$	$9/2^-$
	1075.1(3)	19(1)	1.45(9)	1.18(8)	1.08(10)	1.08(10)	0.65	-1.4(8)	$E2/M1$	$13/2^-$	$11/2^-$
	1226.8(3)	19(1)	1.16(9)	0.97(10)	0.92(12)	1.01(10)			$E2$	$13/2^-$	$9/2^-$
5124(2)	589(1)	0.4(2)									
5314.9(5)	1614.0(5)	4.0(8)	2.06(24)							(11/2)	9/2
5318.6(3)	378.9(2)	3.8(2)	0.58(6)	0.73(19)	0.77(19)	0.92(16)	0.66	-0.06($^{11}_{9}$)	$E2/M1$	$15/2^-$	$13/2^-$
	1454.7(4)	28(1)	1.22(7)	0.94(6)	0.98(6)	1.04(6)			$E2$	$15/2^-$	$11/2^-$
5367.9(3)	427.7(4)	1.0(2)	1.34(35)							$13/2^-$	$13/2^-$
	657.8(3)	2.8(2)	0.58(8)	0.79(26)	0.70(28)	0.81(21)	0.66	0.0(2)	$E2/M1$	$13/2^-$	$11/2^-$
	1183(1)	0.7(3)								$13/2^-$	$9/2^-$
	1343(1)	0.8(2)								$13/2^-$	$9/2^-$
	1505(1)	1.4(3)								$13/2^-$	$11/2^-$
5513.0(3)	194.2(2)	2.0(5)	0.68(10)	0.99(37)	0.83(27)	1.35(45)				$15/2^-$	$15/2^-$
	573.4(2)	34(1)	0.61(4)	0.78(6)	0.64(5)	0.80(5)	0.66	0.00($^{5}_{4}$)	$E2/M1$	$15/2^-$	$13/2^-$
	1649.1(3)	12(1)	1.17(8)	0.98(9)	1.03(12)	0.96(8)			$E2$	$15/2^-$	$11/2^-$

Table 6. Continued

E_x (keV)	E_γ (keV)	I_{rel} (%)	R_{30-83}	R_{DCO} 30°-53°	30°-83°	53°-83°	α_2[a]	$\delta(E2/M1)$ Ass.	Mult. ($\hbar$)	I_i^π ($\hbar$)	I_f^π
5661.2(3)	293.2(2)	2.5(2)	0.46(6)	1.04(35)	0.73(27)	0.76(22)	0.66	0.0(2)	$E2/M1$	$15/2^-$	$13/2^-$
	722.1(4)	1.8(4)	0.85(8)[d]							$15/2^-$	$13/2^-$
	1160.2(2)	7.2(3)		1.09(26)	1.16(34)	1.12(26)			$E2$	$15/2^-$	$11/2^-$
6158.2(6)	843.4(6)	0.9(3)	1.29(21)[d]							(13/2)	(11/2)
	2456(1)	4.3(4)	1.41(26)						($E2$)	(13/2)	9/2
6357.6(8)	845(1)	1.6(6)	0.92(10)[d]	1.08(17)	0.95(17)	1.09(15)		[d]			$15/2^-$
6418.7(4)	757.6(6)	2.4(4)	0.64(38)[d]						($E2/M1$)	$17/2^-$	$15/2^-$
	905.7(2)	21(1)	1.03(6)	1.27(11)	0.96(11)	0.80(8)	0.68	$-3.9\binom{7}{10}$	$E2/M1$	$17/2^-$	$15/2^-$
	1100.1(3)	11(1)	0.25(3)	0.40(6)	0.20(3)	0.56(5)	0.68	$+0.94\binom{18}{13}$	$E2/M1$	$17/2^-$	$15/2^-$
	1480(1)	1.3(3)								$17/2^-$	$13/2^-$
6694(1)	2830(1)	1.9(3)	1.54(20)								$11/2^-$
7038.4(6)	880.0(4)	1.6(3)	0.97(16)							(15/2)	(13/2)
	1723(1)	2.0(3)	1.35(27)							(15/2)	(11/2)
	2098(2)	0.9(2)								(15/2)	$13/2^-$
7142.3(5)	723.1(4)	2.3(5)	0.85(8)[d]	1.27(30)	1.13(29)	0.83(23)		[d]		($17/2^-$)	$17/2^-$
	785(1)	1.5(5)								($17/2^-$)	
	1631(1)	2.5(5)	0.92(11)	1.10(26)	0.56(16)	0.85(16)	0.69	-0.1(2)	($E2/M1$)	($17/2^-$)	$15/2^-$
	1823(1)	0.6(2)						[d]		($17/2^-$)	$15/2^-$
7452.5(4)	1033.5(3)	10(1)		1.17(17)	1.44(27)	1.19(18)	0.70	$-1.2\binom{6}{9}$	($E2/M1$)	$19/2^-$	$17/2^-$
	1939.3(5)	10(1)		0.89(17)	0.97(23)	1.04(21)			$E2$	$19/2^-$	$15/2^-$
	2133.7(6)	3.9(4)		1.05(24)	1.15(28)	0.98(20)		[d]	($E2$)	$19/2^-$	$15/2^-$
7813.7(6)	775.2(4)	3.4(3)								(17/2)	(15/2)
	1656(1)	1.8(3)								(17/2)	(13/2)
	2496(1)	2.8(3)		0.83(25)	0.71(23)	0.67(17)	0.71	0.0(2)	($\Delta I = 1$)	(17/2)	$15/2^-$
8038.2(4)	585.3(3)	1.5(2)	0.68(18)							(19/2)	$19/2^-$
	1621(1)	3.3(5)	[d]							(19/2)	$17/2^-$
	2526(1)	2.2(4)								(19/2)	$15/2^-$
8271(1)	2952(2)	2.2(3)	$\ll 1$								$15/2^-$
8342.9(4)	890.3(3)	5.0(6)		1.42(29)	1.07(25)	0.91(19)			($E2/M1$)	$21/2^-$	$19/2^-$
	1924.4(5)	21(2)		1.01(13)	1.16(17)	1.14(15)		[d]	$E2$	$21/2^-$	$17/2^-$
8548.3(7)	734.7(2)	4.0(2)		0.93(19)	0.73(18)	0.86(16)	0.72	-0.18(12)	$E2/M1$	(19/2)	(17/2)
	1509(1)	0.7(2)								(19/2)	(15/2)
8673(2)	3354(2)	1.4(2)		1.09(42)	0.92(47)	0.86(29)			($E2$)	($19/2^-$)	$15/2^-$
8887.9(9)	545(1)	0.6(2)								($21/2^-$)	$21/2^-$
	1745(1)	4.0(4)		1.19(37)	0.93(30)	1.22(34)			($E2$)	($21/2^-$)	($17/2^-$)
9482.7(7)	934.3(3)	2.7(3)									(19/2)
9494.3(5)	1151.4(4)	4.8(3)		0.87(21)	1.46(62)	1.39(40)			($E2/M1$)	$23/2^-$	$21/2^-$
	2041.6(6)	6.5(5)		1.10(24)	1.24(32)	1.07(27)			$E2$	$23/2^-$	$19/2^-$
9529.7(8)	981.5(5)	1.0(3)									
	1259(1)	0.7(2)									
9855.6(8)	967.5(5)	1.4(4)									
	1818(1)	2.8(3)							[d]		
10210(1)	1867(1)	1.7(3)									
11217(1)	1688(1)	1.2(3)									
	1734(1)	1.4(4)									
11248(1)	1754(1)	0.5(3)								($25/2^-$)	$23/2^-$
	2905(1)	3.7(2)		0.79(17)	1.16(30)	1.06(22)			($E2$)	($25/2^-$)	$21/2^-$
12545(1)	1298(1)	1.3(3)									($25/2^-$)
	2335(2)	1.4(3)									
	3049(3)	0.6(1)									$23/2^-$

[a] The attenuation coefficients were fixed using the relation $\alpha_2 = 0.55 + 0.02 \cdot E_x(\mathrm{MeV})$ and uncertainties $\Delta\alpha_2 \pm 0.05$
[b] Assignment also based on [32]
[c] The spin and parity assignment of this intermediate level is based on a known spin difference of four (six) between the initial and final states of a γ-ray cascade consisting of two (three) transitions assuming that only transitions with $\Delta I \leq 2$ are observed
[d] Doublet structure

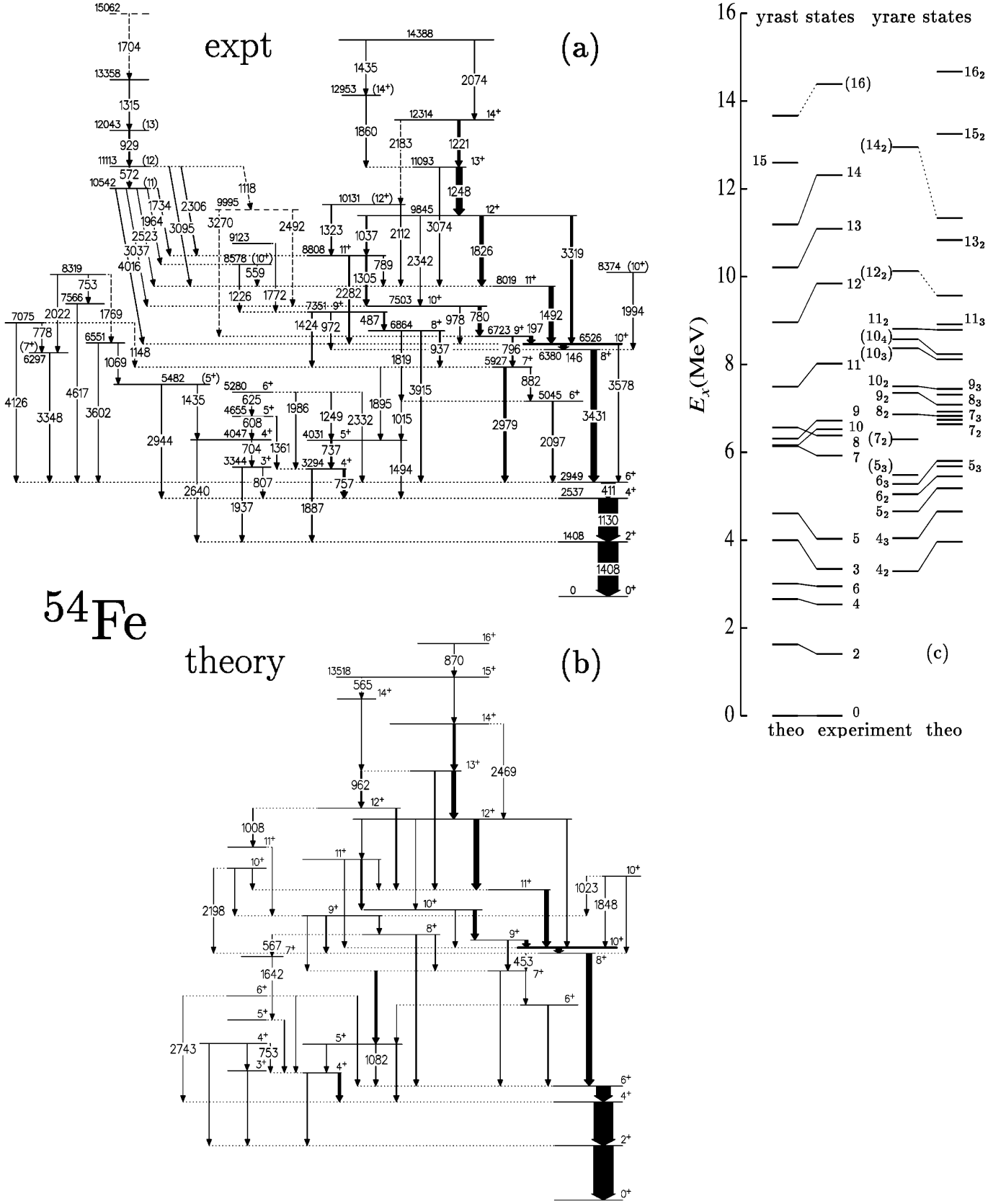

Fig. 3. The proposed partial experimental level scheme of ^{54}Fe is shown in **a**. The energy labels are given in keV. The widths of the arrows are proportional to the relative intensities of the γ rays. Tentative transitions and levels are dashed, **b** illustrates the calculated level scheme using the experimental excitation and γ-ray transition energies and intensity population pattern but calculated transition strengths. Transitions which have *not* been observed but could have been in terms of their predicted yield are labelled with their energy in keV, **c** compares experimental and calculated level energies for the yrast (left) and yrare (right) states. For details see text

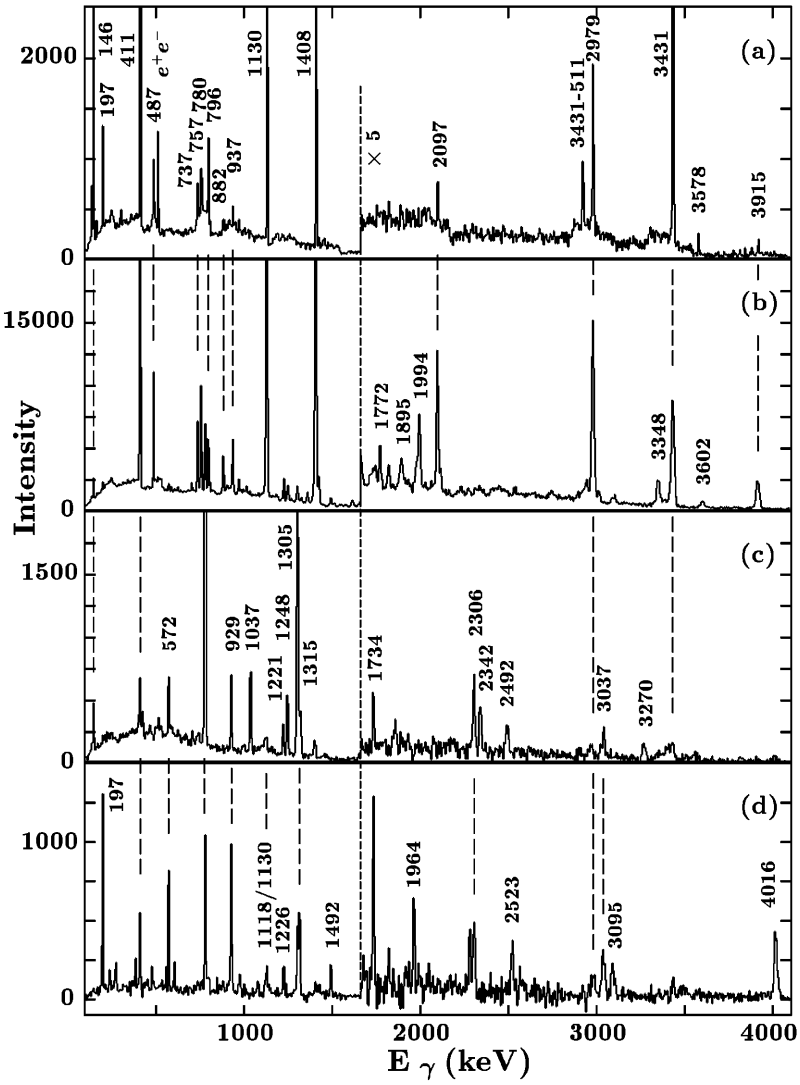

Fig. 4. a–d. Gamma-ray spectra of ^{54}Fe are shown deduced from $\gamma\gamma$ matrices gated by two α particles and two protons: Sum of the spectra in coincidence with the 411, 1130, and 1408 keV transitions ($6^+ \rightarrow 4^+ \rightarrow 2^+ \rightarrow 0^+$ yrast sequence) employing **a** the backed and **b** the unbacked target data. **c** is the spectrum gated by the 197 keV $9^+ \rightarrow 10^+$ yrast transition, **d** the sum of the spectra gated by the 572 and 929 keV transitions ('$M1$' band)

their R_{30-83} values and the existence of the comparatively weak parallel 3 MeV branches. However, the lack of intense stretched $E2$ gating transitions prevented a conventional DCO-analysis of this part of the level scheme. Instead, we used the summed spectra gated by the 197 and 1248 keV stretched $\Delta I = 1$ transitions to gain further evidence for the spin and parity assignments. One expects R_{DCO} values close to unity if the mixing ratios for *both* the gating and analysed transition were small. In fact, this seems to be the case for the transitions of interest which are marked with the tablenote *f* in Table 2. The R_{30-83} value of the upmost 2074 keV transition in this cascade is consistent with an $E2$ assignment based on the previously (cf. Sect. 2) suggested trend of the increasing alignment width σ. However, the lack of additional numbers or arguments prevents a firm spin assignment to the 14388 keV level. This, for example, is possible for the tentative 12^+ assignment to the 10131 keV level. The R_{30-83} values of the 1323 and 2112 keV transitions are consistent with stretched $\Delta I = 1$ transitions, and the tentative feeding 2183 keV line allows only for spin assignments 12 or 13. The latter, however, can be excluded from yrast arguments because the 10131 keV state is only weakly populated though it were yrast by almost 1 MeV in that case.

2.2 Experimental results for $^{54}_{27}$Co$_{27}$

Excited states in ^{54}Co have previously been studied with light ion induced reactions [25]. Above the $I = 0^+$ ($T = 1$) ground state a second β-decaying $I = (7)^+$ state has been observed at 199 keV excitation energy. Other firmly established levels are the $I = 1^+$ and $I = 2^+$ states at 937 and 1446 keV, respectively. The level scheme resulting from our high-spin study is shown in Fig. 5a and summarized in Table 3. The middle panel in Fig. 6 illustrates a "purified" ^{54}Co spectrum. From a $2\alpha 1p1n$-gated γ-ray spectrum leak through from higher-fold charged-particle channels (e.g., ^{53}Fe+$2\alpha 2p1n$ or ^{50}Mn+$3\alpha 1p1n$) was subtracted. Secondly, contaminations arising from small target impurities ($< 0.6\%$ ^{29}Si, $< 0.4\%$ ^{30}Si) were eliminated. For example, transitions from the reaction

Table 7. The energies of excited states in ^{58}Cu, the transition energies and relative intensities of the γ rays placed in the level scheme, angular distribution and the DCO-ratios, and the spins and parities of the initial and final states of the γ rays

E_x (keV)	E_γ (keV)	I_{rel} (%)	R_{30-83}	R_{DCO} 30°-83°	I_i^π ($\hbar$)	I_f^π ($\hbar$)
443.5(2)	443.5(2)	100(3)	1.11(5)	0.90(9)	3^{+a}	1^+
1548.8(3)	1105.0(3)	29(1)	0.47(5)	0.55(10)	4^{+a}	3^+
1646.7(7)	1647(1)	10(1)			3^{+b}	1^+
2064.4(3)	418(1)	8(1)			5^+	3^+
	515.4(3)	26(1)	0.37(3)	0.54(7)	5^+	4^+
	1621.2(4)	60(2)	1.20(8)	1.08(8)	5^+	3^+
2919.6(5)	2476.4(8)	14(1)	1.30(13)	1.17(16)	5^+	3^+
3420.1(5)	500.5(3)	6(1)		1.01(20)	7^+	5^+
	1355.6(4)	75(2)	1.26(8)	1.09(10)	7^+	5^+
3512(2)	592.0(5)	3(1)				5^+
4064.7(6)	1145.2(5)	9(1)	1.23(20)	0.95(30)	(7^+)	5^+
	2000(1)	15(1)	1.39(19)	0.94(32)	(7^+)	5^+
4440.4(6)	1020.4(4)	42(2)	0.91(5)	0.77(12)	8^+	7^+
5189(2)	3125(3)	2(1)				5^+
5346.9(8)	906(1)	8(1)	0.70(17)		9^+	8^+
	1927(1)	33(2)	1.20(10)	1.05(15)	9^+	7^+
5574.0(7)	1509.3(5)	16(1)	1.21(12)			(7^+)
6386.2(9)	1039(1)	5(1)	0.86(17)		10^+	9^+
	1946(1)	24(2)	1.43(16)^c	1.10(16)	10^+	8^+
6585(2)	1396(1)	1(1)				
	3073(3)	2(1)				
6793(1)	1446(1)	6(1)	1.74(34)		(9)	9^+
7391(1)	2044(2)	19(2)	1.35(17)^c	1.22(25)	(11^+)	9^+
8126(1)	1740(1)	12(1)	0.97(15)	0.78(20)	(11)	10^+
8226(1)	2652(2)	4(1)				
	3035(3)	2(1)				
8486(2)	2100(2)	9(1)	1.25(16)	1.34(47)	(12^+)	10^+
8880(2)	1489(1)	5(1)				(11^+)
	2087(2)	4(1)				(9)
8915(1)	2330(2)	1(1)			J	
9679(3)	2288(2)	7(1)				(11^+)
9745(1)	830.2(3)	22(1)	1.13(12)	0.90(24)	$J+2$	J
	1519(1)	5(1)	1.24(34)		$J+2$	
	4171(3)	6(1)	1.46(25)		$J+2$	
9803(1)	1317(1)	4(1)			(12)	(12^+)
	1677(1)	8(1)	0.80(32)	1.22(30)	(12)	(11)
10775(3)	1895(1)	6(1)				
10942(1)	1197.3(5)	30(2)	1.25(11)	1.13(19)	$J+4$	$J+2$
11552(3)	3066(3)	3(1)				(12^+)
11841(2)	2038(2)	6(1)	1.35(17)^c			(12)
12519(1)	1576.4(4)	28(1)	1.41(14)	0.98(12)	$J+6$	$J+4$
13128(4)	2353(2)	3(1)				
14474(2)	1955(1)	24(1)	1.43(16)^c	1.04(22)	$J+8$	$J+6$
14880(4)	3039(3)	3(1)				
16816(3)	2342(2)	16(1)	1.44(16)	1.21(40)	$(J+10)$	$J+8$
19564(3)	2748(2)	8(1)	1.40(23)		$(J+12)^d$	$(J+10)$
22745(5)	3181(3)	2(1)			$(J+14)^d$	$(J+12)$

[a] Assignment also based on [36]

[b] The spin and parity assignment of this intermediate level is based on a known spin difference of four (six) between the initial and final states of a γ-ray cascade consisting of two (three) transitions assuming that only transitions with $\Delta I \leq 2$ are observed

[c] Doublet structure

[d] Assignment suggested by rotational band structure

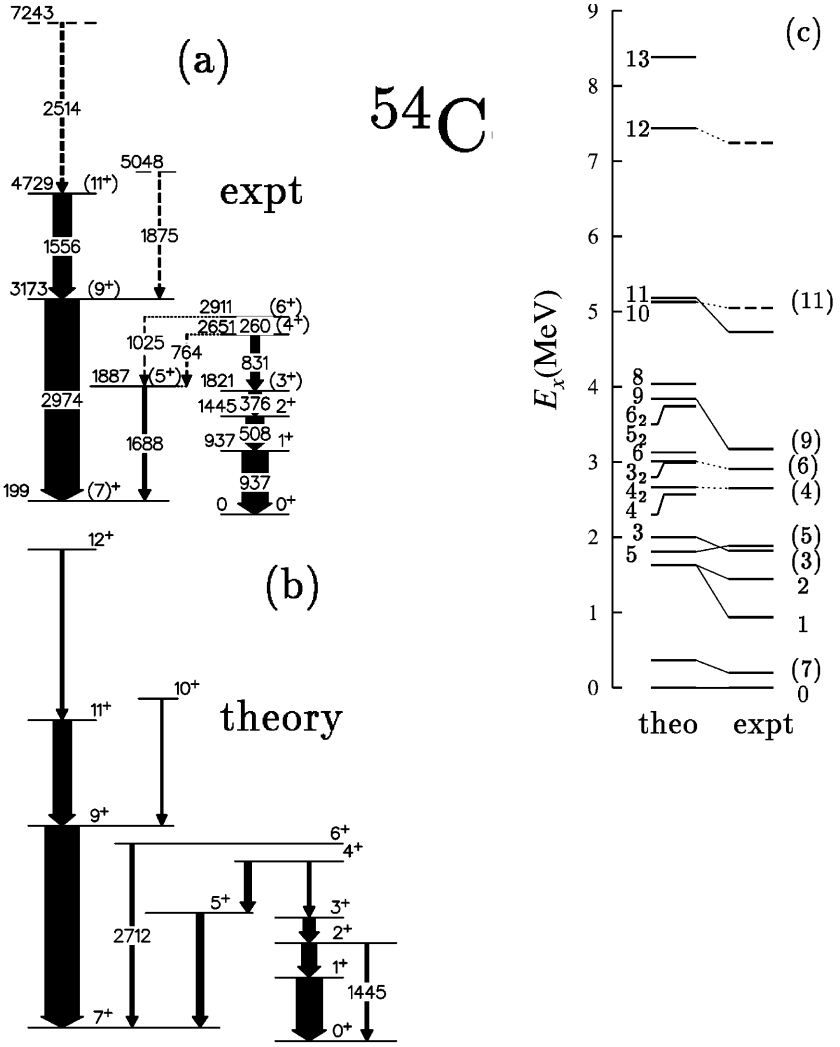

Fig. 5. The proposed partial experimental level scheme of ^{54}Co is shown in **a**. The energy labels are given in keV. The widths of the arrows are proportional to the relative intensities of the γ rays. Tentative transitions and levels are dashed. **b** illustrates the calculated level scheme using the experimental excitation and γ-ray transition energies and intensity population pattern but calculated transition strengths. Transitions which have *not* been observed but could have been in terms of their predicted yield are labelled with their energy in keV. The even-spin members of the $f_{7/2}$ multiplet (0^+, 2^+, 4^+, and 6^+) are $T = 1$ states. Part (c) compares experimental and calculated level energies. For details see text

^{29}Si(^{36}Ar,2α1p1n)^{55}Co could be subtracted by using the spectrum from the main reaction producing ^{55}Co, namely ^{28}Si(^{36}Ar,2α1p)^{55}Co. In fact, for ^{54}Co the latter turned out to be the main source of contamination because the evaporation of an additional particle in excess of those four necessary to populate ^{54}Co is highly unlikely in terms of (excitation) energy.

Next to the known γ rays at 260, 376, 508, 831, (845), 937, and 1688 keV [25] the spectrum in Fig. 6b reveals two distinct peaks at 1556 and 2974 keV. The latter is a doublet with the most intense 2973 keV $11/2^- \rightarrow 7/2^-$ ground-state transition in the ^{55}Co+2α1p reaction channel (see below). Figure 6c presents the spectrum in coincidence with the 2974 keV line in a 2α1p1n gated matrix. Firstly, a coincidence with the 1556 keV transition is obvious, a peak at 1875 keV visible, and one at 2514 keV possible. Secondly, it is noteworthy that transitions originating from ^{55}Co are absent, in particular those at 739 and 801 keV (cf. Fig. 7). This is a clear indication of the extremely good channel selectivity achieved for this experiment which arises from restrictive hard- and software neutron gating. The sudden drop in intensity beyond the 1556 keV line is somewhat surprising, but is probably related to the excitation energy arguments mentioned above.

Due to its very similar energy and large yield we attribute the 2974 keV transition in ^{54}Co with the decay of a core excited $I = (9^+)$ high-spin state upon the $I = (7)^+$ $T = 0$ level. The ratio R_{30-83} for the 1556 keV transition is consistent with stretched quadrupole character, and coincidence relations with the 1875 and 2514 keV lines give rise to the high-spin part of the level scheme on the left hand side of Fig. 5a. Coincidence, intensity, and summed energy relations were used to establish the low-spin sequence of ^{54}Co shown on the right hand side of Fig. 5a. In the upper panel of Fig. 6 the spectrum in coincidence with the 937 keV $1^+ \rightarrow 0^+$ ground-state transition illustrates the 260-831-376-508 keV cascade on top of the 937 keV 1^+ state. In addition, another previously reported line at 845 keV is seen, but could not be established due to low statistics. In a spectrum gated by the 1688 transition small peaks are present at 764 and 1025 keV which are candidates for the decay into the 1887 keV (5^+) state from the 2911 keV (6^+) and 2651 keV (4^+) levels, respectively. These three and the 1821 keV (3^+) state were known

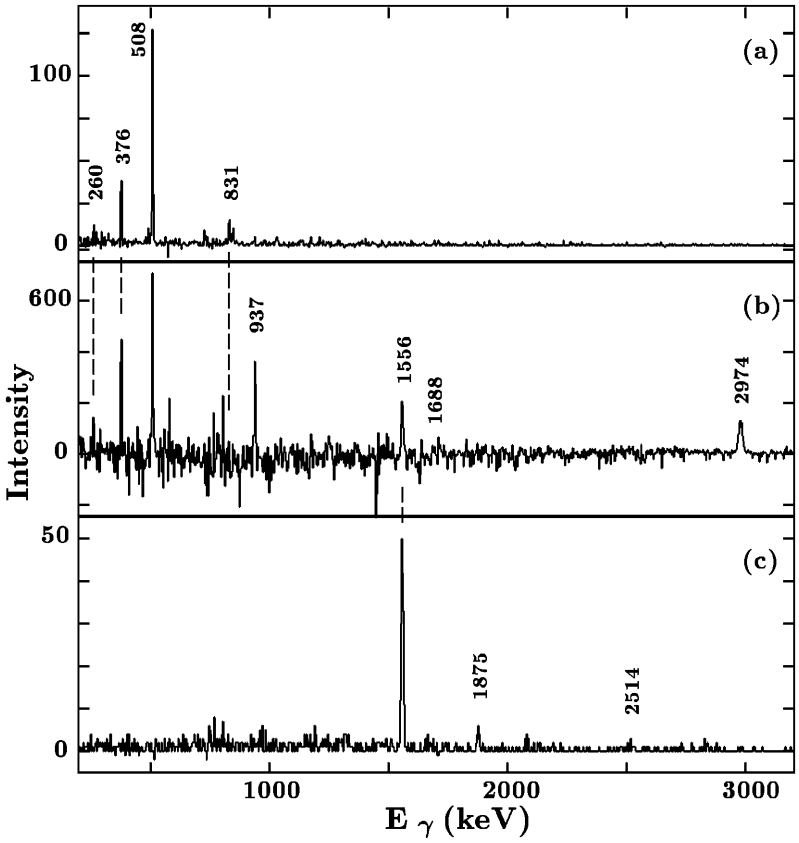

Fig. 6. Gamma-ray spectra of ^{54}Co are shown deduced from $\gamma\gamma$ matrices gated by two α particles, one proton, and one neutron: The spectrum in coincidence with the 937 keV transition ('low-spin' sequence) is shown in **a**, the spectrum in coincidence with the 2975 keV transition ('high-spin' sequence) in part **c**. The middle panel provides the purified $2\alpha 1p1n$ gated projection

[25], and our excitation energies and tentative spin assignments (see Table 3) are consistent with the published numbers. However, in a recent ^{54}Fe(p,$n\gamma$)^{54}Co study [27] the 831 keV transition was found to be a doublet which might lead to a reorder of the γ rays above the 1821 keV state. This sequence, of course, can only be weakly populated in high-spin studies due to yrast arguments.

2.3 Experimental results for $^{55}_{27}$Co$_{28}$

Next to a number of low-spin studies [28] a few high-spin states were previously reported for ^{55}Co, namely a 740-802-2974 keV cascade, tentatively assigned to the $(19/2^-) \rightarrow (15/2^-) \rightarrow (11/2^-) \rightarrow 7/2^-$ yrast sequence [29]. The additional tentative transition of 1951 keV could not be confirmed in the present work and might reflect the double-escape peak of the reported 2974 keV ground-state transition. The other three transitions were confirmed (739, 801, and 2973 keV in the present work) but the spin assignment of the 4514 keV level changed to $I^\pi = 17/2^-$ since the angular distribution analysis, the ratio R_{30-83}=0.93(5), and the DCO-ratios of the 739 keV transition provide a $E2/M1$ transition with a mixing ratio of $\delta = -0.22(4)$ (cf. Fig. 2). In addition, some 100 new transitions have been placed in the extensive level scheme of ^{55}Co shown in Fig. 7a. The information is summarized in Table 4.

Next to the 739-801 keV couple a parallel 778-763 keV sequence via the yrast 3737 keV $13/2^-$ state has been observed. The existence and the intensity of a 38 keV $15/2^- \rightarrow 13/2^-$ transition can be inferred form the coincidence relation between the 739 and 763 keV lines. This is illustrated in Fig. 8a which shows the γ-ray spectrum in coincidence with the 739 keV transition, two alpha particles, and one proton using the backed target data. Figure 8b provides the spectrum of the thin target experiment and the same gating conditions. The 763 keV line is a doublet with the 766 keV $21/2 \rightarrow 19/2^-_4$ transition but the latter is absent in Fig. 8a because the half life of its decay is apparently very fast, thus fully Doppler shifted. The spectrum in Fig. 8a provides additional sharp peaks at 511 keV (e^+e^- annihilation radiation) and 2462 keV (single escape line of the 2973 keV ground-state transition) but also several peaks with a broad pedestal (due to partial Doppler shift) at 857, 1350, 1707, 1752, 2083, 2128, and 3319 keV. As can be seen in Fig. 7a they form the yrast and near yrast cascades between the 9699 keV $25/2^-$ and the 4514 keV $17/2^-$ levels. Because of the presence of both stopped and Doppler-shifted components in the lineshape the (accumulated) lifetimes of the corresponding states have to be on the order of one or two picoseconds.

For the majority of levels below 10 MeV excitation energy the spin and parity assignments are straight forward based on the angular distribution and angular correlation values given in Table 4. Beyond 10 MeV a definite spin *and* parity assignment is possible only for the 10580 keV $25/2^-_2$ level since the mixing ratios of the 1890 and 2231 keV transitions were found to be non-zero. In several other cases

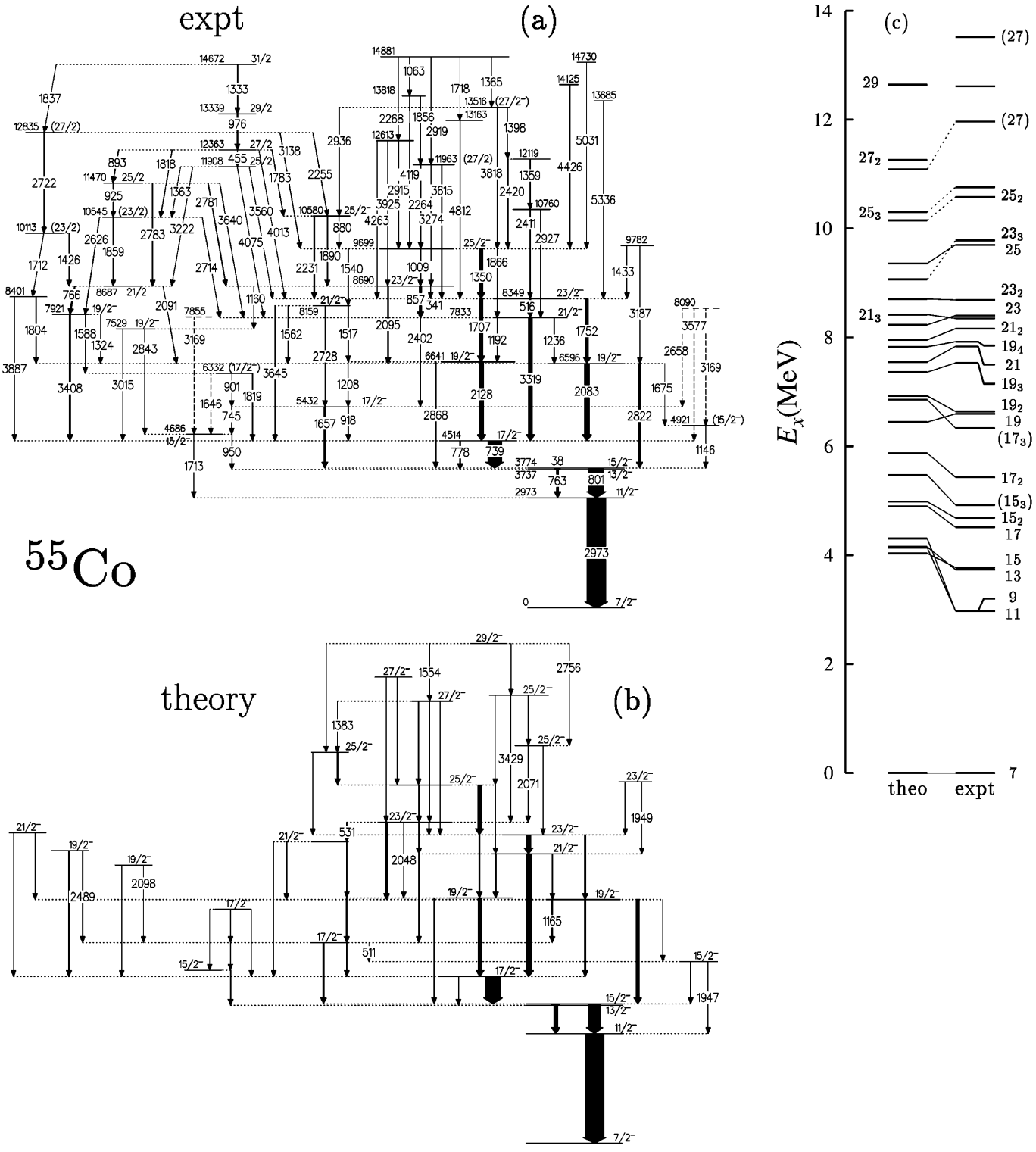

Fig. 7. The proposed partial experimental level scheme of ^{55}Co is shown in **a**. The energy labels are given in keV. The widths of the arrows are proportional to the relative intensities of the γ rays. Tentative transitions and levels are dashed. **b** illustrates the calculated level scheme using the experimental excitation and γ-ray transition energies and intensity population pattern but calculated transition strengths. Transitions which have *not* been observed but could have been in terms of their predicted yield are labelled with their energy in keV, **c** compares experimental and calculated level energies. For details see text

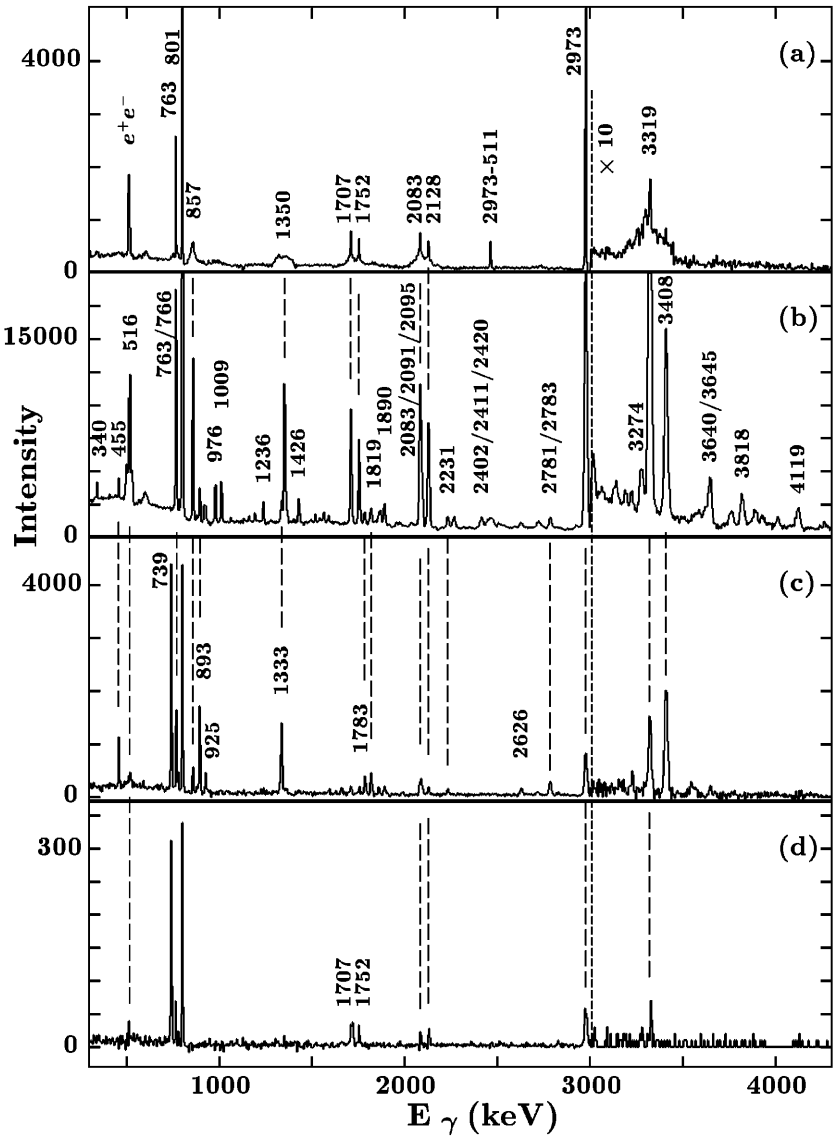

Fig. 8. a–d. Gamma-ray spectra of ^{55}Co are shown deduced from $\gamma\gamma$ matrices gated by two α particles and one proton: Spectrum in coincidence with the 739 keV $17/2^- \rightarrow 15/2^-$ yrast transition employing **a** the backed and **b** the unbacked target data, **c** is the spectrum gated by the 976 keV $29/2 \rightarrow 27/2$ transition, **d** the spectrum gated by the 4812 keV transition

(e.g., the 766 keV $21/2 \rightarrow 19/2^-_4$ or 1783 $27/2 \rightarrow 25/2^-_2$) the mixing ratios are consistent with zero and, hence, no definite parity assignments are possible for a number of states on the left hand side of Fig. 7a. The additional argument to fix the parity, namely to attribute $\Delta I = 2$ transitions solely with $E2$ character, might be dangerous as one expects comparatively strong $M2$ connections in this mass region between the $g_{9/2}$ and $f_{5/2}$ orbits [30]. They would give rise to weak but observable $M2$ branches through preferably high energy γ rays such as, possibly, the 4013 or 4075 keV transitions.

Similar to the regular structure found in ^{54}Fe the levels at 11908, 12363, 13339, and 14672 keV might form a regular $\Delta I = 1$ sequence. Though the average difference in γ-ray energy supports such an assignment, the additional decay of the top-most level via the 1837 keV transition speaks against it. Figure 8c provides the spectrum in coincidence with the 976 keV $29/2 \rightarrow 27/2$ line showing that this sequence is comparatively strongly populated, i.e., there is sufficient statistics to not only establish firm coincidence relations high up in the ^{55}Co level scheme but to perform a reliable angular correlation analysis as well. The latter is no longer possible for the weakly populated high-spin structures on the right hand side of Fig. 7a: as an example, the spectrum in coincidence with the 4812 keV transition is illustrated in Fig. 8d. Though statistics are low, the coincidence relations are undoubtful because, e.g., even the weak 516-3319 keV branch out of the 8349 keV $23/2^-$ state can be observed in Fig. 8d.

2.4 Experimental results for $^{56}_{28}$Ni$_{28}$

The highlights of the results in ^{56}Ni from the present experiment are published separately [10]. They include the observation of two rotational bands one of which is likely to have a some 50% prompt proton decay branch into the ground state of ^{55}Co. Light ion induced reactions [1] have been previously used to establish the yrast line up to a

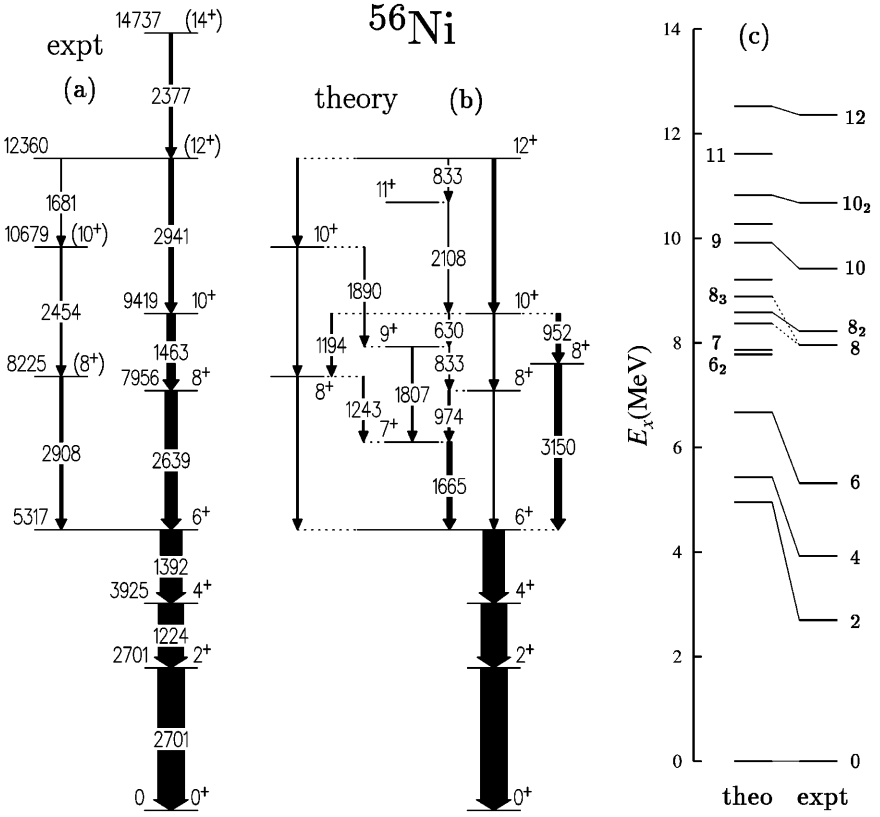

Fig. 9. A partial experimental level scheme of ^{56}Ni is shown in **a**. The rotational bands [10] are not shown. The energy labels are given in keV. The widths of the arrows are proportional to the relative intensities of the γ rays, **b** illustrates the calculated level scheme using the experimental excitation and γ-ray transition energies and intensity population pattern but calculated transition strengths. Transitions which have *not* been observed but could have been in terms of their predicted yield are labelled with their energy in keV. **c** compares experimental and calculated level energies. For details see text

level at 9419 keV which was tentatively associated with the yrast 10^+ state [31]. We confirmed this work and extended the spherical part of the ^{56}Ni level scheme to some 15 MeV excitation energy and spin $I = 14$. In addition, yrare (8^+) and (10^+) states were identified as illustrated in Fig. 9a. Up to the 9419 keV state firm spin and parity assignments were feasible. The ratios R_{30-83} and/or the DCO-ratios for the 2377, 2908, and 2941 keV transitions are consistent with stretched $E2$ transitions as well. For the sake of simplicity, the deformed states in ^{56}Ni have not been included in Fig. 9a but in Table 5 which summarizes our present high-spin knowledge on ^{56}Ni.

2.5 Experimental results for $^{57}_{28}$Ni$_{29}$

Until recently, excited states in ^{57}Ni were studied only by proton, ^{3}He, or α-particle induced reactions [32]. Next to numerous low-spin states ($I = 1/2$–$9/2$) above the $3/2^-$ ground state, the high-spin yrast cascade was followed up to the $15/2^-$ state at 5318 keV excitation energy [29]. In a study employing the Osiris γ-ray spectrometer coupled to a recoil filter detector this crude excitation scheme was extended to a state at 8345 keV with a spin assignment of 19/2, and including a number of yrare states in the 3–6 MeV excitation energy regime [33]. Except for the spin assignment of the (here:) 8343 keV state (which turns out to be $21/2^-$) our excitation scheme presented in Fig. 10a is in perfect agreement with [33]. Some 60 transitions were added which mainly connect newly identified yrare levels but also extend the excitation energy to some 13 MeV. The results are summarized in Table 6. It should be noted that a preliminary analysis of data from another Gammasphere experiment indicates the presence of a (super)deformed rotational band in ^{57}Ni at even higher excitation energies [34].

Figure 11 shows γ-ray spectra gated with one α-particle, two protons, and one neutron in coincidence with (a) the 768 keV ground-state transition, (b) the sum of the low-spin 1287 and 2577 keV intense yrast transitions, (c) the high-spin 1151 keV $23/2^- \rightarrow 21/2^-$ transition, and (d) the 1124 keV transition depopulating the 3701 keV state which is the daughter state of the ^{58}Cu prompt proton decay (see below). Panel (a) employs the backed target data while panels (b), (c), and (d) arose from the data taken with the thin target. Figure 11a mainly illustrates the weakly populated yrare levels on the left hand side of Fig. 10a. The $15/2^-$ states and possibly those of lower lying states have lifetimes in excess of a picosecond since the connecting transitions do not show any sign of Doppler shifted components. Figure 11b shows the plethora of γ rays associated with ^{57}Ni, and Fig. 11c selects the yrast cascade. Note that in this panel the tentative weak 1754 and 3049 keV transitions are present. Finally, Fig. 11d shows the line in connection with the right hand side of the ^{57}Ni level scheme. In addition to transitions from ^{57}Ni, the γ rays from the well-deformed, proton decaying band in ^{58}Cu are present at 830, 1197, 1576, 1955, and 2342 keV. They are marked with a filled circle. It should be noted

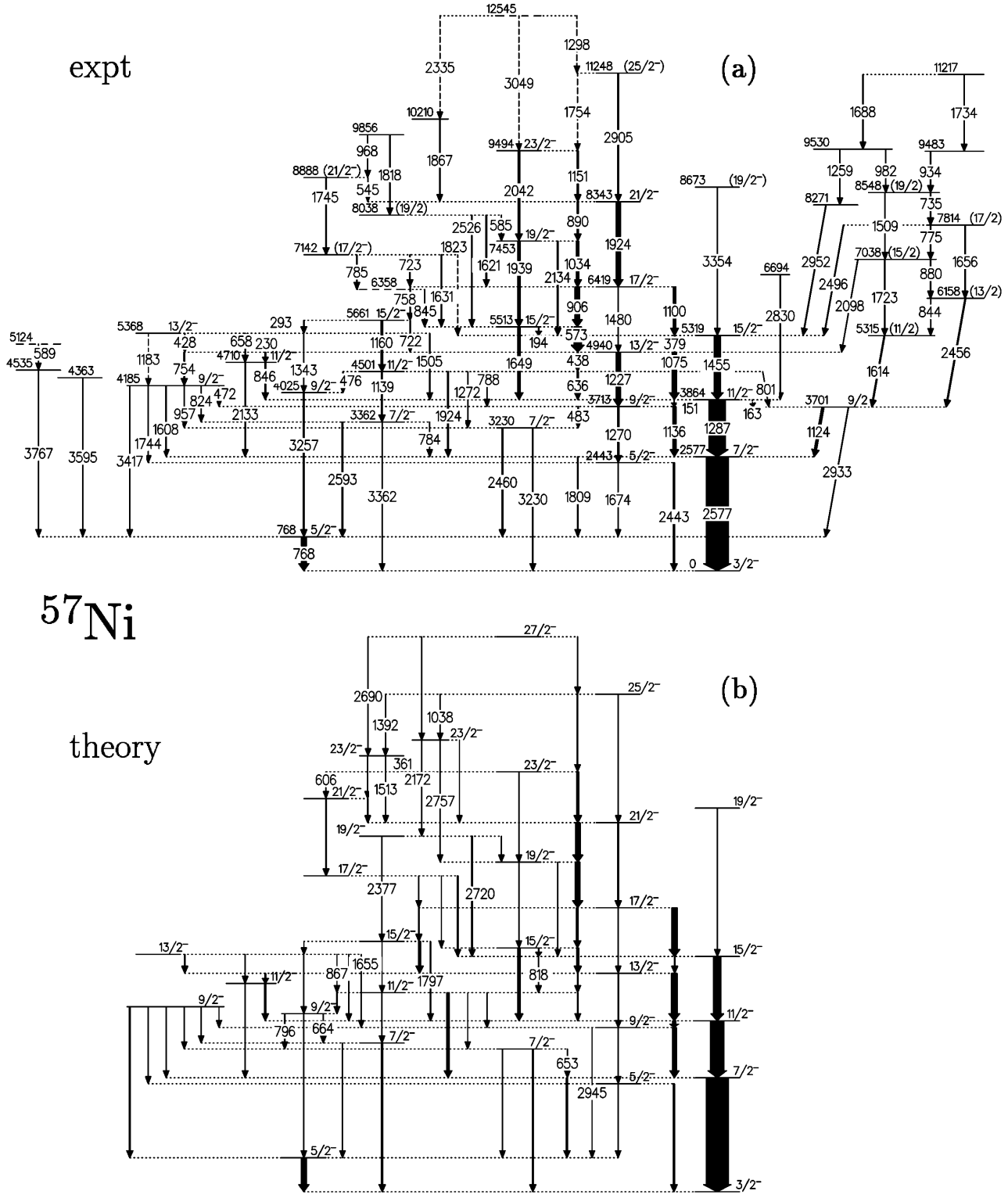

Fig. 10. The proposed partial experimental level scheme of ^{57}Ni is shown in **a**. The energy labels are given in keV. The widths of the arrows are proportional to the relative intensities of the γ rays. Tentative transitions and levels are dashed. **b** illustrates the calculated level scheme using the experimental excitation and γ-ray transition energies and intensity population pattern but calculated transition strengths. Transitions which have *not* been observed but could have been in terms of their predicted yield are labelled with their energy in keV. For details see text

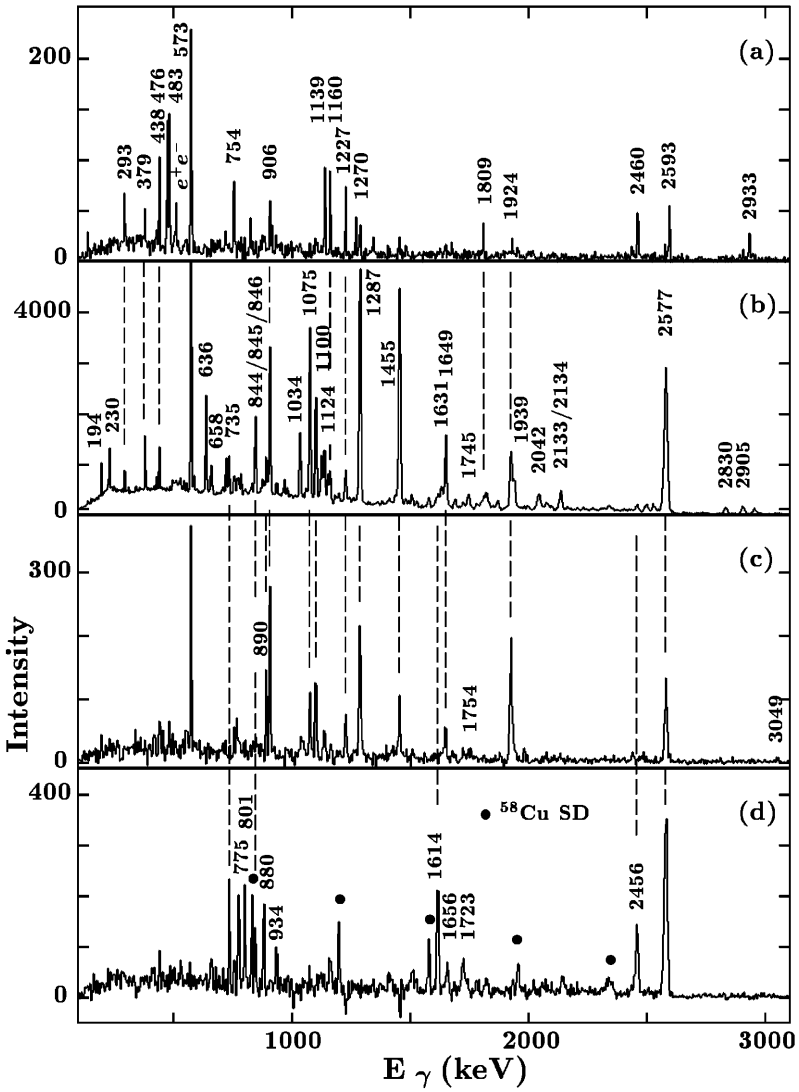

Fig. 11. a–d. Gamma-ray spectra of ^{57}Ni are shown deduced from $\gamma\gamma$ matrices gated by one α particle, two protons, and one neutron: Spectrum in coincidence with the 768 keV $5/2^- \rightarrow 3/2^-$ ground-state transition employing the backed target data **a**. **b** shows the sum of spectra in coincidence with the 1287 and 2577 keV transitions ($11/2^- \rightarrow 7/2^- \rightarrow 3/2^-$ yrast sequence), **c** corresponds to the spectrum gated by the 1151 keV $23/2^- \rightarrow 21/2^-$ yrast transition, **d** the spectrum gated by the 1124 keV transition. The 1124 keV transition depopulates the daughter state of the prompt proton decay of ^{58}Cu. Hence, the transitions from the corresponding rotational band [4] are present, marked with •

that in the backed target data the 1124 keV transition is stopped, while all other higher-lying transitions in Fig. 11d provide distinct Doppler-shifts.

The combination of previous low- and high-spin results [32,33] and the present angular correlation and angular distribution analysis leads to definite spin and parity assignments of almost all states below 6 MeV excitation energy. There are, however, inconsistencies between the low-spin particle spectroscopy and the high-spin γ-ray data with respect to the assignments of the "doublet" at 3701 and 3713 keV excitation energy. The latter state has tentative positive parity assigned in [32] while the previous and present high-spin study consistently yield $9/2^-$. Our assignment is mainly based on the angular correlation coefficients of the 1136 keV $9/2^- \rightarrow 7/2^-$ transition (see Table 6). This is illustrated in the third column of Fig. 12 which provides the angular distributions (first row), the associated χ^2 analysis of the mixing ratio δ (second row), and the analysis of the mixing ratio δ based on the most sensitive DCO-ratio R_{DCO}(30-83) (third row) for a multiplet of stretched $\Delta I = 1$ transitions at some 1120 keV and the stretched $E2$ 1227 keV $13/2^- \rightarrow 9/2^-$ line. The lines through the data points in the first row are least squares fits to the angular distribution formula (1). The middle, slightly thicker curves in the χ^2 plots correspond to the analysis with the calculated (see above) width σ of the Gaussian magnetic substate distribution. At the top of each column the corresponding alignment coefficient α_2 is given. The thinner curves represent calculations with the upper and lower limit of σ while the grey shaded areas indicate possible solutions for the mixing ratio δ. From the combined angular distribution and correlation analysis we deduce a non-zero mixing ratio $\delta = -0.15(9)$ for the 1136 keV transition, hence mixed $E2/M1$ character, i.e., negative parity and spin $I = 9/2$ for the 3713 keV state.

In the evaluation of [32] the 3701 keV state has a spin-parity assignment of $I^\pi = (5/2)^-$. The previous high-spin study, however, allows $I = 7/2$ or $9/2$ but no parity assignment [33]. This level represents the (so far) exclusively populated daughter state of the prompt proton decay from the second minimum of ^{58}Cu (see below and [4]). Therefore, we paid special attention to the analysis

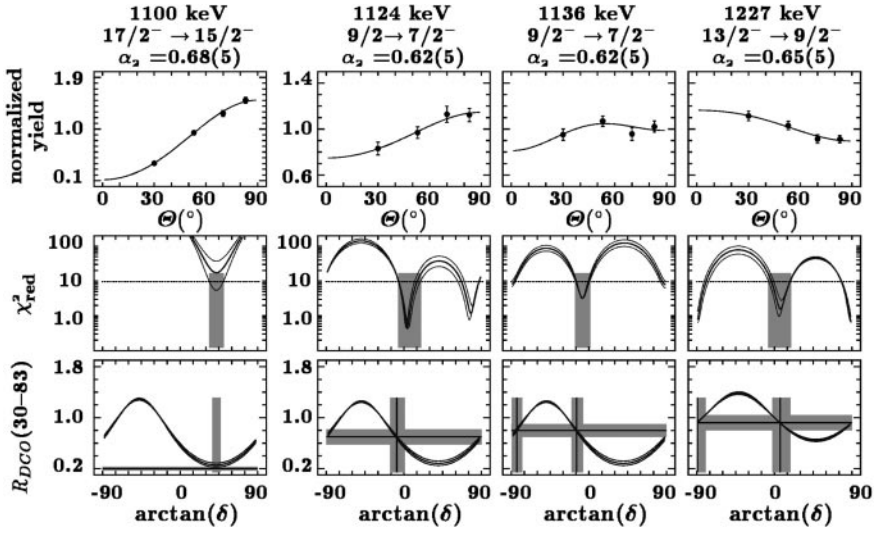

Fig. 12. The angular distribution and correlation analysis of four transitions in ^{57}Ni is presented. The first row illustrates least squares fits of Legendre polynomials according to formula (1). The middle row shows the associated χ^2 analysis of the mixing ratio δ. The thicker curves correspond to the analysis with the calculated width σ of the Gaussian magnetic substate distribution. At the top of each column the corresponding alignment coefficient α_2 is given. The thinner curves represent calculations with the upper and lower limit of σ while the grey shaded areas indicate possible solutions for the mixing ratio. In the third row the mixing ratio deduced from the most sensitive DCO-ratio R_{DCO}(30-83) is shown (cf. Fig. 2)

of the 1124 keV γ ray, illustrated in the second column of Fig. 12. This transition carries most of the flux out of the 3701 keV level, and its multipolarity was found to be of stretched $\Delta I = 1$ character. An $I = 5/2$ assignment for the 3701 keV state is highly unlikely because of yrast arguments: The level is more strongly populated in ^{57}Ni *itself* (only some 6(1)% of the yield of the 1124 keV transition is due to the proton decay) than, e.g., the first excited $I = 5/2^-$ state at 2443 keV. Therefore, we assign a spin $I = 9/2$ to the 3701 keV state, in agreement with [33]. However, the deduced mixing ratio of the 1124 keV transition is consistent with zero, i.e., we cannot distinguish between stretched $M1$ or $E1$ character, thus we cannot fix the parity of the 3701 keV state with the present data set. Nevertheless, three arguments favor positive parity for that level. Firstly, two $I^\pi = 9/2^-$ states only 12 keV apart seem not very reasonable due to level repulsion. Secondly, in the odd-A neighbors ^{59}Ni and ^{59}Cu $g_{9/2}$ single-particle states have been observed at 3.1 MeV excitation energy [35]. Thirdly, the rotational band in ^{58}Cu is most likely based on a deformed $[\pi g_{9/2} \otimes \nu g_{9/2}]_{9^+}$ configuration [4], and the angular distribution of the emitted proton suggests a large angular momentum associated with the decay, i.e., likewise the proton in the $g_{9/2}$ orbit. In turn, this leaves a single neutron in the $g_{9/2}$ orbit, and we associated the 3701 keV level with the $\nu g_{9/2}$ *spherical* single particle state. If the 3701 keV state had a distinct quadrupole deformation we should have observed a rotational band on top of it, which we have not [see Fig. 10a]. Nevertheless, the parity of the 3701 keV state needs to be determined in future experiments. The $I^\pi = 9/2^+$ assigment would lead to an $M2$ assignment to the weak 2933 keV branch out of the 3701 keV state. Since this γ ray would connect the $g_{9/2}$ and $f_{5/2}$ neutron single particle states of the ^{56}Ni core, it should resemble the strongest $M2$ decay possible in the mass region [30].

Definite spin and parity assignments of a few more yrast levels beyond 6 MeV excitation energy were feasible, but for most of the higher lying transitions only tentative multipolaritiy assignments were possible due to reduced statistics. The unusually large R_{30-83} value of the 1614 keV line feeding the 3701 keV state could be explained by a large negative $E2$ admixture of a stretched $\Delta I = 1$ transition similar to the 2231 keV $25/2^- \rightarrow 23/2^-$ transition in ^{55}Co.

2.6 Experimental results for $^{58}_{29}$Cu$_{29}$

Similar to ^{56}Ni, the highlights of our results concerning ^{58}Cu were published separately [4]. A well-deformed rotational band ($\beta_2 \approx 0.37$) was observed which deexcited both by γ decay into the spherical states of ^{58}Cu, and by prompt discrete proton emission into the spherical 3701 keV 9/2 level in ^{57}Ni (see above). Prior to our investigation, only few well characterized low-spin levels were known from mainly proton or ^{3}He induced reactions on ^{58}Ni targets [36]. As already stated in [4] the level scheme shown in Fig. 13 is built upon the previously identified 444, 1105, and 1647 keV transitions. The other reported γ rays, mainly related to the even spin $T = 1$ ^{58}Ni isobaric analogue states, are about 1 MeV above the yrast line and, hence, not accessible in our high-spin study.

Up to the 3420 keV 7^+ state the level scheme is dominated by a strong $E2$ cascade consisting of the 444, 1621, and 1356 keV transitions, accompanied by three weaker "bypasses". Thereafter, a sequence of $\Delta I = 1$ (1020, 906, and 1039 keV) transition is crossed over by stretched $E2$ transitions, and finally the level scheme of the spherical states splits into several weak branches reaching a maximum excitation energy of some 15 MeV. Spin and parity assignments are straight forward up to the 6386 keV 10^+ level based on the numbers presented in Table 7. Using the ratios R_{30-83} the spins of several more states were suggested, including the 4065 keV (7^+) level which forms the main basis for the linking transitions from the second into the first minimum of the potential. The ratio $R_{30-83} = 1.21(12)$ of the 1509 keV transition on top of that state might suggest a spin $I = (9)$ for the 5574 keV state. A definite spin assignment as well as the confirma-

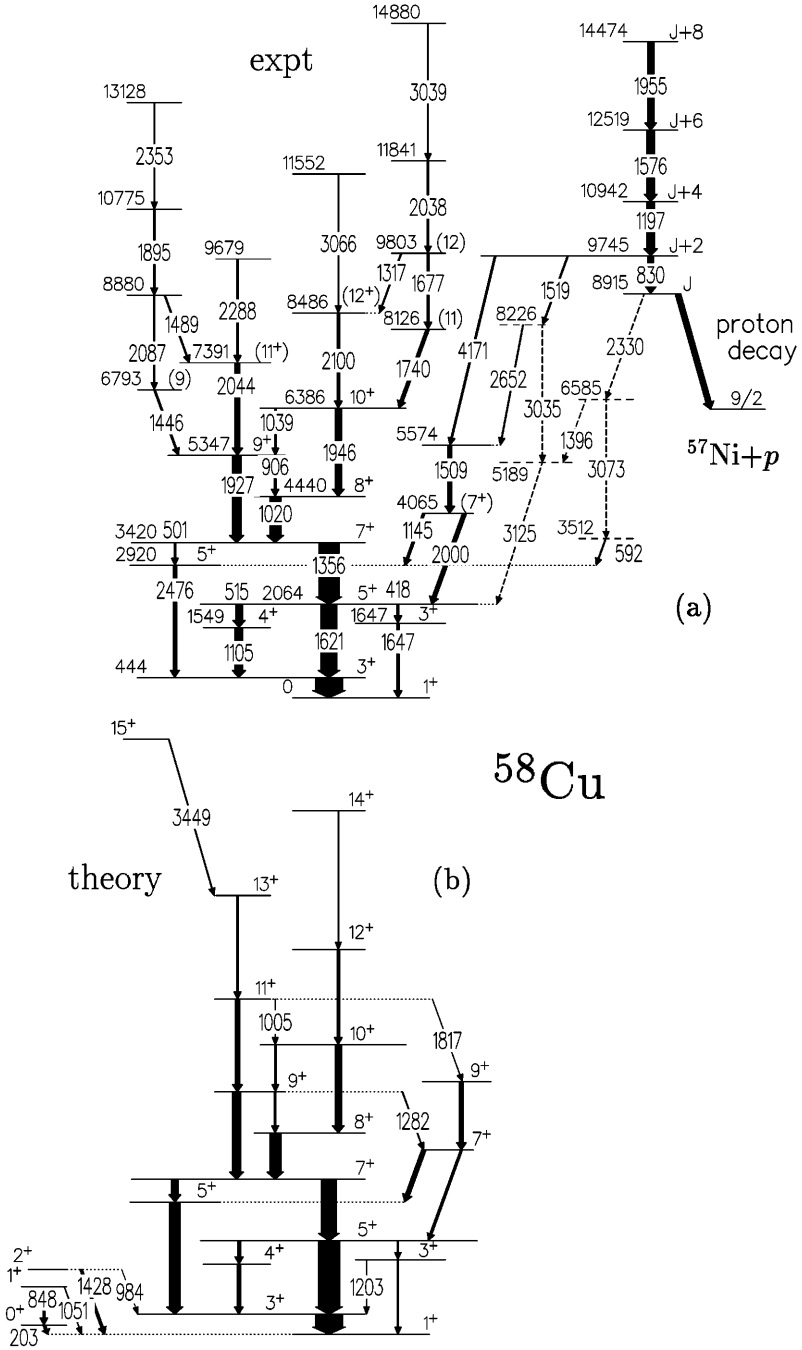

Fig. 13. a The proposed partial level scheme of ^{58}Cu [4] **a**. The high-spin part of the rotational band and the γ decay of the 3701 keV ^{57}Ni daughter state are not shown. **b** illustrates the calculated level scheme using the experimental excitation and γ-ray transition energies and intensity population pattern but calculated transition strengths. Transitions which have *not* been observed but could have been in terms of their predicted yield are labelled with their energy in keV. For details see text. The three states in the lower left corner have been seen in low-spin studies. The 0^+ and 2^+ levels are $T = 1$ states

tion of several very weak other potential γ-ray links await improved statistics from upcoming experiments.

3 Discussion

The interpretation of excited states in the vicinity of a doubly magic nucleus clearly calls for the spherical shell model. The orbits involved near ^{56}Ni are the $1f_{7/2}$ orbit below and the $2p_{3/2}$, $1f_{5/2}$, and $2p_{1/2}$ (upper fp shell) orbits above the N,$Z = 28$ shell gap. For this so-called full fp model space two common parameter sets exist, namely the FPD6 interaction by Richter, van der Merwe, Julies, and Brown [37], and the KB3 interaction introduced by the Madrid-Strasbourg group [38]. Employing the rapidly increasing computer power and more sophisticated diagonalization algorithms [39], the deformed $N \approx Z$ nuclei in the mid $1f_{7/2}$ shell (up to mass $A = 50$) could recently be well explained by large-scale full fp shell-model calculations [40–44].

Unfortunately, the current computational limit for calculations in the full fp configuration space are mass $A = 52$ nuclei [45] with basis dimensions in excess of 100 million states. Therefore, the configuration space for cal-

culations in the direct vicinity of ^{56}Ni must be truncated at present: For the recent study of the rotational bands in ^{56}Ni the excitation of up to six particles from the $1f_{7/2}$ into the upper fp shell was allowed (basis dimension of some 25 million states), and the calculations proved very successful in explaining one of the rotational bands with a four-particle four-hole (4p-4h) structure [10].

More recent developments try to make a detour around the problems associated with such huge dimensions in the model space by tracing the most significant components via Monte-Carlo methods. These Shell-Model Monte-Carlo (SMMC) [46] and Quantum Monte-Carlo Diagonalisation (QMCD) [47,48] calculations were very successful in describing, e.g., ground state properties of the fp shell nuclei [49] or the spherical yrast sequence in ^{56}Ni [50]. The average number of particles occupying the $1f_{7/2}$ shell was found to be ~ 14 for the spherical shell-model states and ~ 10 for the first rotational band in ^{56}Ni [51].

However, excited particles moving in the high-j $1g_{9/2}$ intruder orbit are necessary to form the strongly or superdeformed bands in the mass region [3,4,10]. Moreover, the $1g_{9/2}$ states have been identified in ^{59}Cu and ^{59}Ni [35] and probably in ^{57}Ni as well (see Sects. II.E and III.F). Therefore, attempts should be made to incorporate this shell in the present fp model space. Of course, this would imply an additional immense increase in the dimensions for the conventional shell-model studies, such that a considerable truncation in the number of particles (i) crossing the N,$Z = 28$ gap and (ii) being excited into the $1g_{9/2}$ orbit will be unavoidable. Thus the SMMC and QMCD models may provide the favorable tools for this implementation.

These up-front theoretical and complicated investigations are beyond the scope of the present study. Instead, we performed rather simple shell-model calculations with the code RITSSCHIL [52]. Based on the above mentioned results of the QMCD calculations [50,51] we allow only up to two particles to be excited across the N,$Z = 28$ shell gap. This keeps the dimension of basis states below some 30000 for all nuclei studied (^{54,55}Fe, ^{54,55,56}Co, ^{55,56,57}Ni, and ^{57,58}Cu), and enables a comprehensive study of not only excitation energies but also electromagnetic decay properties. We used the FPD6 parameter set for the two-body residual interaction, and our single-particle energies are based on recent results from Trache *et al.* [53] ['TRA' in Fig. 14a]. These authors deduced the "bare" single-particle energies in ^{56}Ni by coupling (mainly vibrational) collective core excitations to the closed ^{56}Ni core which arise from strong $E2$ correlations between the $1f_{7/2}$ and $2p_{3/2}$ orbits across the shell gap which soften the doubly magic core considerably [54]. Since these collective excitations are not included in pure shell-model calculations, we first carefully modified the single particle energies of the upper fp shell such that the $3/2^-$ ($2p_{3/2}$ orbit) ground states and first excited $5/2^-$ ($1f_{5/2}$ orbit) and $1/2^-$ ($2p_{1/2}$ orbit) states in the mass $A = 57$ mirror pair ^{57}Cu [32] and ^{57}Ni were reproduced within some 10 keV. This was achieved by lowering the $\pi 1f_{5/2}$ and $\nu 1f_{5/2}$ by approximately 1 MeV with respect to the $2p_{3/2}$ shells. As

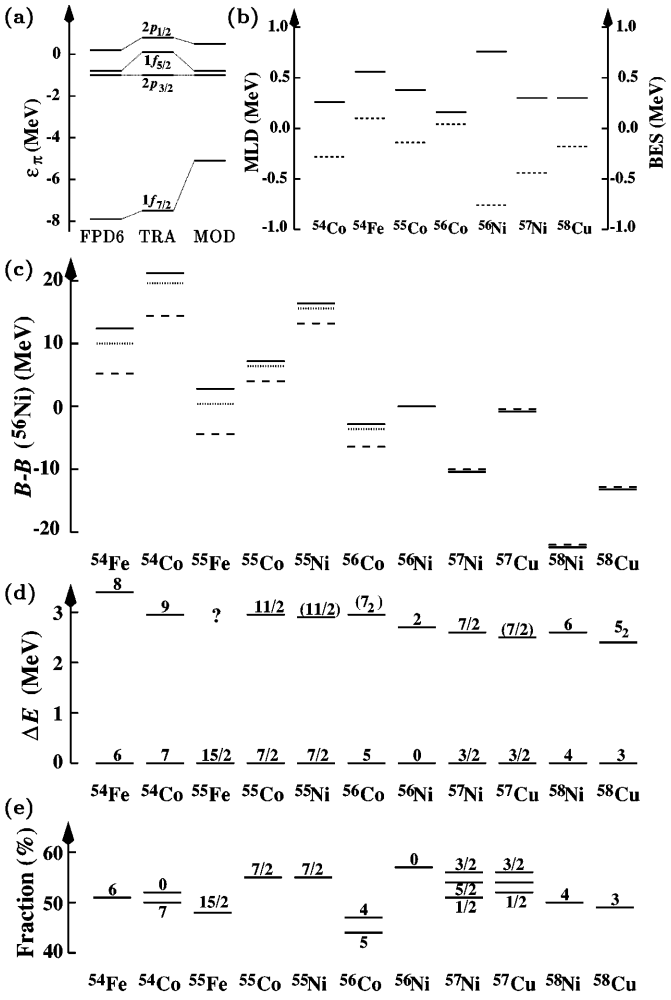

Fig. 14. a–e. An overview of general shell-model quantities is presented. In **a** we show the single-particle energies (SPE) from the original FPD6 parameter set [37], the "bare" single-particle energies deduced in [53], and those used in the present calculations. In panel **b** one finds the mean level deviations (MLD) and binding energy shifts (BES) of the investigated nuclei. **c** illustrates the experimental (solid lines) and calculated (dashed) binding energies of several nuclei around ^{56}Ni, **d** provides a glance over the experimental $E2$ core excitation energies while in panel **e** the percentage of closed core partitions in the wave functions are shown

a consequence, the splitting used between these two orbits is very similar to the value suggested for the slightly modified single-particle energies of the original FPD6 parameter set (when moving from ^{40}Ca towards ^{56}Ni) [37, 55] ['FPD6' in Fig. 14a]. In a second step, the gap between the upper fp shell and the $1f_{7/2}$ orbit was lowered by 2.4 MeV to account for the softness of the core, and to reproduce the excitation energy of the (presumably) stretched 2p-2h $[(\pi f_{7/2}^{-1} \otimes \nu f_{7/2}^{-1})_{7^+} \otimes (\pi p_{3/2} \otimes \nu p_{3/2})_{3^+}]$ 10^+ and $[(\pi f_{7/2}^{-1} \otimes \nu f_{7/2}^{-1})_{7^+} \otimes (\pi f_{5/2} \otimes \nu f_{5/2})_{5^+}]$ 12^+ yrast states in ^{56}Ni ['MOD' in Fig. 14a]. The numbers are summarized in Table 8. Similarly, the KB3 interaction gives a too large gap at particle numbers 28 [56]. This has led

Table 8. "Experimental" single-particle energies in MeV from Ref. [53] and the ones used in the present Ritsschil calculations for the ^{40}Ca and ^{56}Ni cores and the FPD6 two-body matrix-elements [37]

	Ref. [53]		present study	
shell	^{40}Ca core	^{56}Ni core	^{40}Ca core	^{56}Ni core
$\nu 1f_{7/2}$	−8.17	−16.93	−5.75	−14.51
$\nu 2p_{3/2}$	−7.65	−10.36	−7.65	−10.36
$\nu 1f_{5/2}$	−1.16	−9.53	−2.10	−10.47
$\nu 2p_{1/2}$	−6.39	−8.48	−6.72	−8.81
$\pi 1f_{7/2}$	1.27	−7.49	3.69	−5.07
$\pi 2p_{3/2}$	1.72	−0.99	1.72	−0.99
$\pi 1f_{5/2}$	8.50	0.13	7.56	−0.81
$\pi 2p_{1/2}$	2.93	0.84	2.60	0.51

to a modified so-called KBF interaction for which all diagonal matrix elements connecting the $1f_{7/2}$ orbit with the others are more attractive by 100 keV. To describe the electromagnetic properties we used effective charges $e_\pi = 1 + \delta e_\pi = 1.33e$ and $e_\nu = 2\delta e_\pi = 0.67e$ [37,57, 58] and effective g-factors $g_{eff} = 0.9 g_{bare}$. The transition strengths were calculated using the experimental γ-ray energies.

3.1 General notes

Next to the single-particle energies, Fig. 14 provides some global features of the comparison between the shell-model calculations and the experimental data. The solid lines in panel (b) reflect the mean level deviations (MLD), the dashed lines the binding energy shift (BES) which is necessary to provide the optimum MLD. The peaking of the MLD for ^{56}Ni itself and the very small MLD for the particle-hole nucleus ^{56}Co provide the first evidence that more (quasiparticle) pair correlations act across the gap than incorporated in our truncated model. Energetically ^{56}Ni is still predicted to be a good doubly-magic core ($E_x(2^+) = 4955$ keV) though the wave functions indicate a distinct weakeness of the core (see below). In Fig. 14c the calculated and experimental [59] binding energies are plotted relative to the ^{56}Ni core. The solid lines correspond to the experimental, the dashed lines to the calculated numbers. Clearly, there is an excellent agreement for the $A \geq 57$ nuclei. However, for each hole relative to $N = Z = 28$ some 3.4 MeV binding energy is missing for the lighter nuclei. This is indicated by the dotted lines for which we have added 2.4 or 4.8 MeV, respectively, to the calculated values to account for our (artificial) 2.4 MeV squeeze of the gap. Nevertheless, the trend within each family (two, one, or zero holes) is nicely reproduced. Figure 14d shows the assigned "closed core" states in several nuclei and the associated energies necessary for the respective core excitation. Below the shell gap this energy amounts to some 3.0 to 3.5 MeV while it is reduced by some 500 keV for nuclei with valence particles in the upper fp shell. Therefore, these nuclei are likely to have more pronounced $E2$ correlations across the gap leading to the somewhat reduced "gap energy". The presence of such correlations is elaborated in Fig. 14e which provides the size of the partition of the "closed core" configuration in the wave functions of the final states shown in panel (d). On average they barely amount to 50% which is a surprisingly small value for presumed pure shell-model or even single-particle states (^{57}Cu, ^{57}Ni). However, it is in accordance with recent results from Monte-Carlo shell-model calculations [50]. Otsuka and co-workers compute 53% for the closed core component of the ^{56}Ni ground state while it amounts to 86% in the case of ^{48}Ca, i.e., the "magicity" of ^{56}Ni is weakened considerably.

Table 9. Measured [60,61] and predicted electromagnetic moments near ^{56}Ni

Isotope	I^π	μ (μ_N)		Q (eb)	
	($\hbar$)	expt	theo	expt	theo
^{54}Fe	2^+	+2.40(34)	+2.34	−0.05(14)	−0.18
	6^+	8.22(18)	+7.82		
	10^+	+7.281(10)	+6.42	+0.291(25)	+0.51
^{55}Co	$7/2^-$	+4.822(3)	+4.62		
^{56}Co	4^+	3.856(12)	+3.31	+0.25(9)	+0.24
^{57}Ni	$3/2^-$	0.88(6)	−1.13		
		−0.7975(14)			

We also calculated the few measured electromagnetic moments in ^{54}Fe [22–24], ^{55,56}Co, and ^{57}Ni [60]. They are summarized in Table 9. While the magnetic moments for states in the lighter nuclei are predicted to be a little bit too small (92% on average) the value for the ^{57}Ni ground state is overpredicted by nearly 30%, i.e., the chosen effective g-factors provide a good compromise. It is interesting to note that the measured magnetic moment ($|\mu| = 0.88(6)\ \mu_N$) of the ^{57}Ni ground state is less than half the Schmidt value ($\mu = \mu_{\text{free neutron}} = -1.91\ \mu_N$) [61,62]. Recently its sign could be determined in a precise nuclear magnetic resonance experiment on oriented nuclei [61]. Prior to that the experimental value was deduced only from ratios of yields of γ rays following the β decay of ^{57}Ni, detected parallel and perpendicular to an applied external magnetic field in an low-temperature nuclear alignment measurement, its sign could not be extracted [62]. The electric quadrupole moments of the 2^+ state in ^{54}Fe and the ground state of ^{56}Co are in agreement with the experimental values. The value for the isomeric 10^+ state, however, is overpredicted. In contrast, the calculated lifetime ($\tau = 673$ ns) for this isomer is larger than the measured one [$\tau = 525(10)$ ns], i.e., the effective charges used provide a good compromise as well.

In Figs. 3b, 5b, 7b, 9b, 10b, and 13b we present "calculated" level schemes which are based on the experimental excitation energies and side-feeding patterns but employing the calculated transition strengths. They are shown next to the experimentally deduced excitation schemes to allow for an immediate visual comparison. Gamma-ray transitions which were predicted with a relative intensity in excess of the typical observational limit for the respective reaction channel are added in the panels (b) labelled

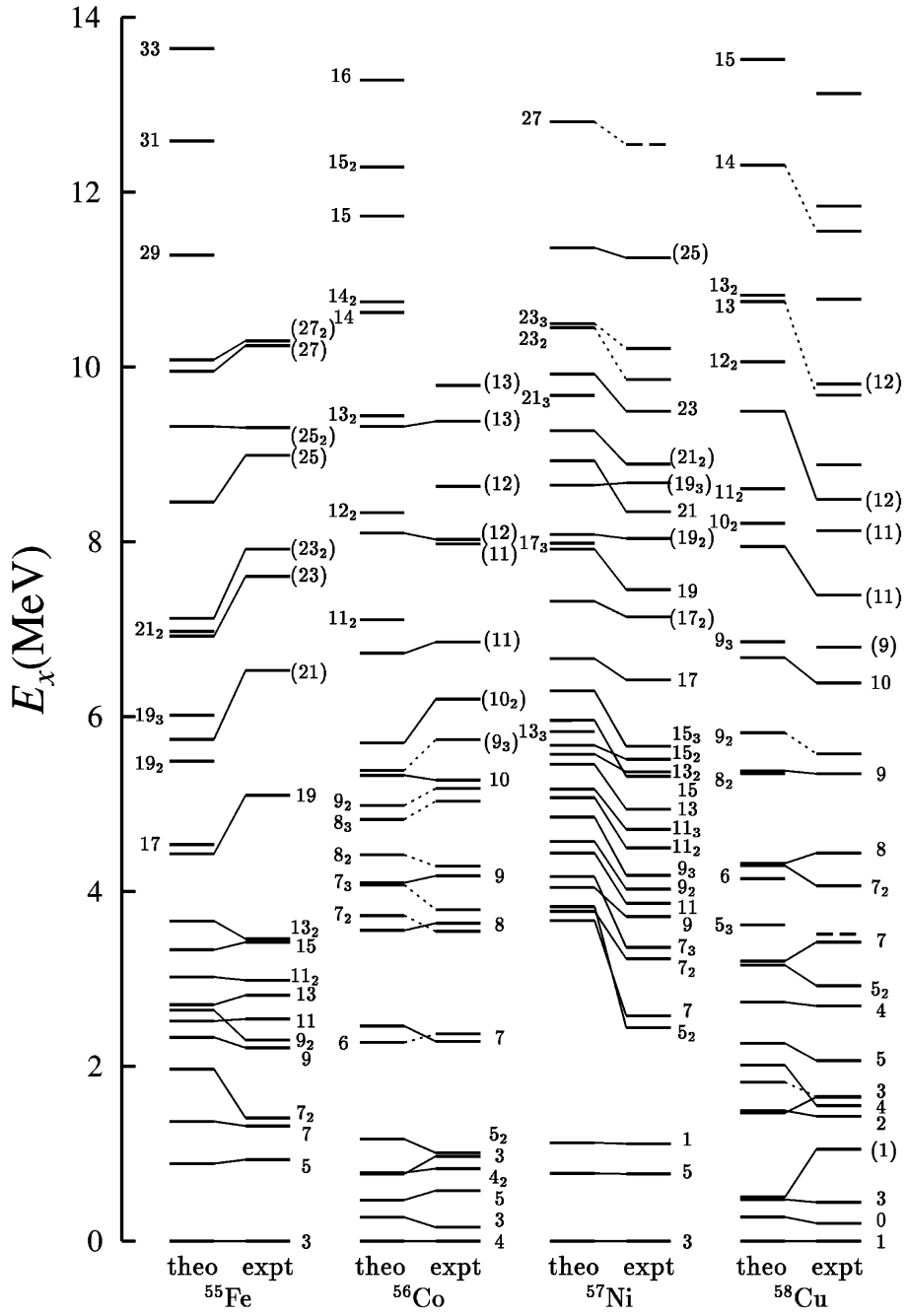

Fig. 15. Experimental and calculated excitation energies of the $N = 29$ series ^{55}Fe, ^{56}Co, ^{57}Ni, and ^{58}Cu are compared

with their energies in keV. Structures which could not be explained by the shell-model calculations were removed. The comparisons might lead to 'shell-model assignments' to experimental levels based on similarly predicted and observed decay patterns. However, these 'assignments' are purely theoretical, i.e., should not be taken as experimental spin and parity assignments to the respective levels. Figures. 3c,5c,7c, 9c, and 15 compare the experimental and theoretical level energies. Tentative experimental levels are dashed, and tentative assignments between observed and calculated levels dotted. Otherwise, they are connected by thin solid lines. In the following subsections, the "calculated" level schemes, the energy comparisons, and important partitions in the wave functions are discussed separately for the different isotopes.

3.2 Calculations and comparisons for ^{54}Fe

The calculated even-spin yrast sequence up to the 2949 keV 6^+ state is in very good agreement with experiment for both excitation energies [cf. Fig. 3c] and transition strengths. The measured lifetimes [25] are 1.15(4), 5.8(12), and 1753(22) ps for the 2^+, 4^+, and 6^+ states,

respectively, which have to be compared to the calculated 1.8, 6.0, and 2129 ps. The wave functions of the states in this sequence are dominated, as expected, by the configurations $\pi(f_{7/2})^{-2}_{0,2,4,6}$, in each case comprising some 50%.

The next group of yrast levels ($I = 7$–11) is characterized by 3h-1p configurations with one neutron being excited across the $N = 28$ gap such as $\pi(f_{7/2})^{-2}_{4,6} \otimes \nu(f_{7/2})^{-1} \otimes \nu(p_{3/2})$, with typical partitions of some 40%. The predicted lifetime of the 10^+ isomer is only 1.3 times the experimental value (see above), and the lifetimes for the other states agree nicely with experiment, too: the 9^+ state should live 18 ps which implies that the lower-lying transitions (197, 796, 882, 2979 keV) should be emitted after the recoils came to rest in the backed target experiment [cf. Fig. 4a]. However, the predicted (accumulated) lifetime for the 11^+ state is less than 0.2 ps, i.e., the 1492 keV $11^+ \rightarrow 10^+$ transition should be completely Doppler shifted. The only major discrepancy is the decay of the 7^+ state which is predicted to proceed mainly via the 1895 keV transtition while it is observed via the 2979 keV transition.

To create higher spin states, the excitation of a second particle across the gap is necessary. For the 12^+–16^+ states this particle is predicted to be a second neutron. For example, the wave function of the 12^+ state has a total of 53% in the configuration $[\pi(f_{7/2})^{-2}_6 \otimes \nu(f_{7/2})^{-2}_6]_{12}$ with the two neutrons in the upper fp shell coupled to spin zero. The yrast 16^+ state is dominated (95%) by the coupling of this four-hole structure to an aligned $[\nu(p_{3/2}) \otimes \nu(f_{5/2})]_4$ configuration. The also possible $\nu(f_{5/2})^2_4$ coupling dominates the second 16^+ state which is predicted about 1 MeV higher in excitation energy. The third possibility involves an underlying $[\pi(f_{7/2})^{-3}_{15/2} \otimes \nu(f_{7/2})^{-1}_{7/2}]_{11}$ structure coupled to $[\pi(f_{5/2}) \otimes \nu(f_{5/2})]_5$. The corresponding level is predicted 2 MeV above yrast. The deduced branching ratios of the 12^+–14^+ yrast states are in excellent agreement with the observations [cf. Fig. 3b] but their excitation energies are calculated about one MeV too low. This, however, might be related to the artificial lowering of the size of the gap — the generation of high-spin states involves the breaking of several nucleonic pairs, i.e., the correlations across the shell gap which are present in the ground state are reduced with increasing seniority. Their strong feeding clearly identifies the 12^+–14^+ states as being yrast and the decay pattern clearly associates them with the calculated yrast levels. However, in the experiment we do miss either the 15^+ or 16^+ state, and the corresponding part of the positive-parity yrast sequence is not well reproduced.

The wave functions of the 7^+_2, 8^+_2, 9^+_2, 10^+_2, and 11^+_2 levels have similar partitions as those of the yrast levels but with a significantly higher fraction of a neutron in the $1f_{5/2}$ instead of the $2p_{3/2}$ shell. Like them the 6^+_2 state is of seniority $v = 4$ and the decay properties and excitation energies of all these levels are very well reproduced. The lifetime of the 7351 keV 9^+_2 level is calculated to be 0.6 ps, i.e., an effective lifetime on the order of $\tau_{\rm eff} = 1$ ps is expected. This is in accordance with the small "pedestal" of the 487 keV transition in Fig. 4a. The yrare 12^+ and 14^+ states have leading components of the $[\pi(f_{7/2})^{-3}_{15/2} \otimes \nu(f_{7/2})^{-1}_{7/2}]_{11}$ hole type. While the decay of the 14^+_2 state is well reproduced, the decay of the 12^+_2 is only reasonably well described, and the excitation energies are predicted to be too high, just like the yrast states.

Several more low-spin ($I =$ 3-6) states were identified and the predictions for them illustrated in the lower left corner of Fig. 3b. Again, the major decay paths are well described while the calculated energies are now too high. This can be considered as an indicator for vibrational admixtures. The mean branching deviation (MBD) [63] for the levels discussed amounts to 0.14(1). This underlines the globally good description of the electromagnetic decay properties (cf. [63]) in ^{54}Fe.

Two sequences in the experimental level scheme of ^{54}Fe [left hand side of Fig. 3a] cannot be described with our model. In particular, we associate the regular sequence at high spin to a so-called $M1$ or "shears" band [64]. In the mass $A \approx 60$ region we expect these bands from the coupling of $1f_{7/2}$ holes to $1g_{9/2}$ particles. As a consequence, the whole high-spin part of the level scheme might be influenced by contributions involving one or two $1g_{9/2}$ particles, and may explain the discrepancies found in, e.g., the decay of the 14388 keV state.

3.3 Calculations and comparisons for ^{54}Co

As can be seen from Figs. 5b and c the overall agreement between the calculated and experimental level scheme and excitation energies is very good. There are only a few but noteworthy differences: Firstly, the high-spin core-excited 9^+ state is calculated somewhat too high which reflects the lack of $E2$ correlations in the shell-model space. The observed (tentative) even-spin level energies are in excellent agreement with both the calculation and the $T = 1$ isobaric analogue states in ^{54}Fe (cf. Fig. 3). However, the decay of the 6^+ state is predicted to proceed via the strong 2712 keV isovector $M1$ transition into the 199 keV 7^+ state rather than through the suggested 260 keV transition into the 4^+ state. Similarly, this 4^+ is expected to decay mainly into the 5^+ state but is observed to also decay via the 831 keV $4^+ \rightarrow 3^+$ line. A $T = 0$ 4^+ state is predicted close to the $T = 1$ 4^+ level. However, its decay shall proceed through an excited 3^+ level which we do not observe experimentally.

Most interestingly, however, the $T = 0$ $I^\pi = 1^+$ deuteron-hole like structure in ^{54}Co is predicted 700 keV too high in energy. In fact, this could be interpreted as enhanced $T = 0$ correlations being present in this odd-odd $N = Z$ nucleus. By making the corresponding $\pi(f_{7/2}) \otimes \nu(f_{7/2})$ diagonal two-body matrix-element 900 keV more attractive the problem, of course, can be cured. However, the question remains whether such a drastic change in the residual interaction can be justified by one single state since the energies of the other seven levels of the $1f_{7/2}$ multiplet are well described. This aspect is interesting to be studied in more detail but it is beyond the scope of the present work. From the experimental point of

view there is an obvious need for more data on both high- and low-spin states in ^{54}Co to allow for a more comprehensive and detailed study.

3.4 Calculations and comparisons for ^{55}Co

The predicted and observed energy levels of the one-proton-hole nucleus ^{55}Co and their decay properties are compared in Figs. 7b and c. At low excitation energies there is a multiplet of yrast $9/2^-$-$15/2^-$ levels predicted around 4 MeV. The $9/2^-$ and $11/2^-$ states are observed about 1 MeV lower which once more can be attributed to the missing collective correlations across the gap. While these levels possess two leading components ($\sim$ 20%), namely $\pi(f_{7/2})_6^{-2}\otimes\pi(p_{3/2})$ and $[\pi(f_{7/2})^{-1}\otimes\nu(f_{7/2})^{-1}]_7\otimes\nu(p_{3/2})$, the $13/2^-$ and $15/2^-$ are dominated ($\sim$ 50%) solely by the latter. The branching ratios are well reproduced. The $13/2^-$ state has a predicted lifetime of nearly 10 ps while the $15/2^-$ shall be comparatively long-lived with $\tau = 650$ ps, in agreement with the sharp peaks of the corresponding γ rays in Fig. 8a.

The yrast $17/2^-$ state is predicted to not only have a sizeable $[\pi(f_{7/2})^{-1}\otimes\nu(f_{7/2})^{-1}]_7\otimes\nu(f_{5/2})$ partition (31%) but also to contain a significant fraction of several 3h-2p components ($\sim$ 30%). This is surprising because in a naive seniority picture one would expect that state to represent a rather pure fully stretched $[\pi(f_{7/2})^{-1}\otimes\nu(f_{7/2})^{-1}]_7\otimes\nu(p_{3/2})$ configuration (here: only 25%), especially because some additional 2 MeV of excitation energy are necessary to form the yrast $19/2^-$ level. In a similar manner, that level should be based on a fully stretched $[\pi(f_{7/2})^{-1}\otimes\nu(f_{7/2})^{-1}]_7\otimes\nu(f_{5/2})$ configuration. However, the present calculation yields only an 8% partition of that type in the yrast but 35% for the (experimentally) nearby yrare $19/2_2^-$ state. In fact, the leading components of the yrast $19/2^-$ state are the stretched 3h-configurations $[\pi(f_{7/2})^{-2}\otimes\nu(f_{7/2})^{-1}]_{19/2}$ or $[\pi(f_{7/2})^{-1}\otimes\nu(f_{7/2})^{-2}]_{19/2}$ with the two particles in the upper fp shell coupled to spin zero (total $\sim$ 55%). Experimentally the two $19/2^-$ state are only 45 keV apart. This hints to a much smaller mixing of the two major stretched 19/2 components (either 2h-1p or 3h type) because the calculated energy difference between the first two $19/2^-$ states amounts to nearly half a MeV. In principle, small changes in the single-particle energies might have a large effect on the size of these components in such closely lying states. As such, the related decay strengths could be altered significantly, i.e., the discrepancy between the observed (mainly mixed $E2/M1$) and predicted (mainly stretched $E2$) decay of the yrast $19/2^-$ state might easily vanish.

This argument holds also true for the yrast and first excited $21/2^-$ and $23/2^-$ states. They all are based on the two stretched $19/2^-$ configurations within the $1f_{7/2}$ orbit with the $[\pi(f_{7/2})^{-2}\otimes\nu(f_{7/2})^{-1}]_{19/2}$ type being slightly preferred. The two remaining particles in the upper fp shell then have a variety of energetically more or less equivalent possibilities to couple to spins one, two, or higher. The excitation energies and branching ratios are well reproduced except for a theoretically strongly favored 516 keV $23/2^- \rightarrow 21/2^-$ yrast transition. In order to reproduce the branching into the two $19/2^-$ states, we tried to apply an additional two-level mixing (mixing coefficient $\alpha = 0.50$) for the wave functions of the two $23/2^-$ levels. Though the strength of the 516 keV line was barely affected, not only the relative branchings of the 1708 and 1753 keV transitions were much better described but also the feeding into the $23/2^-$ levels. (In Fig. 7b the results for the mixed $23/2^-$ states are presented.) The lifetime of the modified yrast $23/2^-$ state is calculated to $\tau = 2.1$ ps which is in accordance with the experimental observations in Fig. 8a which show stopped and Doppler shifted components for the parallel 1708-2128 and 1752-2083 keV cascades. The 857 keV transition which depopulates the yrare $23/2_2^-$ state has only a small stopped component remaining, in agreement with the predicted lifetime of $\tau = 0.9$ ps. The lifetimes of the higher lying states are calculated to be significantly smaller than one picosecond. To apply such an additional level mixing is, of course, not in line with a pure shell-model approach: The mixing can be due to either inadequate two-body matrix-elements or single-particle energies (see, e.g., the notes in Sect. 3.6). In addition, configurations from outside the model space might be of importance. However, any of such modifications would require the investigation of their impact on the full set of calculations which is beyond the present approach.

The calculations for the yrast $25/2^-$ state yield three about equal ($\sim$ 25%) partitions with the configurations $[\pi(p_{3/2})\otimes\nu(p_{3/2})]_3$, $[\pi(f_{5/2})\otimes\nu(p_{3/2})]_4$, and $\nu(f_{5/2})_4^2$ coupled to the respective stretched $19/2^-$ 'three-hole basis'. However, the first excited $25/2^-$ state has a 60% $[\pi(f_{7/2})^{-2}\otimes\nu(f_{7/2})^{-1}]_{19/2}\otimes[\pi(p_{3/2})\otimes\nu(p_{3/2})]_3$ partition and, according to its excitation energy and decay pattern, is associated with the level at 10580 keV. Similarly, the 10760 keV is probably the $25/2_3^-$ level. As can be seen from Fig. 7a the experimental level scheme highly fragments beyond the yrast $25/2^-$ level and, due to the then small intensities of the γ rays, only a few tentative spin and parity assignments were possible on the upper right hand side of the figure. The predicted decay scenario starts from the fully aligned 3h-2p $29/2^-$ state and provides four nearly equally weak branches. This forking is, hence, in agreement with the fragmented experimental decay scheme. However, the only state which seems to fit the predicted depopulation and the excitation energy [cf. Fig. 7c and the $25/2^-$ states] is the one at 13516 keV — but that state has a tentatively assigned spin of $27/2^-$. In addition, the states at 11963 keV (assigned tentative spin 27/2) and 12613 keV nicely agree with the predicted decay pattern of the yrast and yrare $27/2^-$ states. Similarly, those at 10760 and 12119 keV might be interpreted as the third and fourth $25/2^-$ states. Finally, these levels are located in an excitation energy regime for which excitations into the high-j $1g_{9/2}$ intruder orbital are likely to occur. In fact, the levels in the upper left part of the experimental ^{55}Co level scheme and their associated decay patterns cannot be satisfactorily reproduced with our

calculation either. The regular 455-976-1333 keV sequence occurs at similar excitation energies and spins as the 572-929-1315 keV cascade in ^{54}Fe and, hence, is another candidate for a $M1$ band. Positive parity for these states implies the presence of three $M2$ transitions (γ rays at 3640, 4013, and 4075 keV) which can be explained by decays from $1g_{9/2}$ into $1f_{5/2}$ components in the wave functions of the respective levels.

Finally, it is worth noting that the three $15/2^-$ states follow the single-particle energies in the sense that the $2p_{3/2}$ neutron particle in the yrast $15/2^-$ state (see above) is exchanged for a $1f_{5/2}$ neutron for the second and a $2p_{1/2}$ neutron for the third $15/2^-$ state. Due to its 'correct' excitation energy and decay pattern we associate the 8401 keV level with the calculated $21/2^-_3$ level.

The MBD of some 20 levels with experimentally known or suggested spins and parities and more than one energetically possible decay branch amounts to 0.10(1). This clearly indicates an overall very good description of the decay pattern in ^{55}Co. The comparison between the excitation energies shows similar features as the results for ^{54}Fe, namely slightly too large predicted values at low and too small values at high spin.

3.5 Calculations and comparisons for ^{56}Ni

As stated above and visualized in Fig. 9c the first three excited even-spin yrast levels in ^{56}Ni are predicted too high in energy. In particular, the 2^+ core excited state with more than 2 MeV in excess of the experimental value. On the contrary, the calculated strength $B(E2; 2^+ \rightarrow 0^+) = 80\ e^2\mathrm{fm}^4$ is within reach of the measured number 120(24) $e^2\mathrm{fm}^4$ [65]. The predicted lifetimes for the 4^+ and 6^+ states are 6 and 4 ps, respectively, and agree with the observation of sharp 1224 and 1392 keV line in the spectra of the backed target set.

The highest spin possible for ^{56}Ni within our restricted model space is the $[\pi(f_{7/2})^{-1} \otimes \nu(f_{7/2})^{-1}]_7 \otimes [\pi(f_{5/2}) \otimes \nu(f_{5/2})]_5$ 12^+ state ($\tau \sim 1$ ps). The decay of that state is split into three transitions which shall populate the yrast 10^+ (55%), the 10^+_3 (35%), and the yrast 11^+ (10%) states. Since the 10^+_2 and 10^+_3 states lie close in energy ($\Delta E <$MLD) and because the decay pattern of the latter (main branch into the 8^+_2 level) matches the observations much better, we associate the calculated 10^+_3 with the observed (tentative) 10^+_2 state at 10679 keV. Its wave function consists of three major partitions, namely $[\pi(p_{3/2}) \otimes \nu(f_{5/2})]$ (30%), $[\pi(f_{5/2}) \otimes \nu(p_{3/2})]$ (23%), and $[\pi(f_{5/2}) \otimes \nu(f_{5/2})]$ (17%) for the proton and neutron in the upper fp shell. In contrast, the calculated 10^+_2 state is dominated by the $[\pi(p_{3/2}) \otimes \nu(p_{3/2})]$ partition (76%) and, hence, has essentially no $E2$ overlap with the 12^+ state: $(B(E2; 12^+ \rightarrow 10^+_2) = 0.2\ e^2\mathrm{fm}^4$. The yrast 10^+ state is a mixture of these four possibilities but governed by the $[\pi(f_{5/2}) \otimes \nu(f_{5/2})]$ type (36%). Nevertheless, the large phase space (~ 3 MeV) allows for a significant decay branch.

The predicted feeding from the 12^+, 10^+_3 and 8^+_2 levels into the yrast odd-spin sequence shown in the middle of Fig. 9b is weak, i.e., the corresponding γ rays are on the edge of our current observational limit. However, if we assign the calculated yrast 8^+ state with the observed one, we should have seen a strong $\Delta I = 1$ $8^+ \rightarrow 7^+ \rightarrow 6^+$ cascade with γ rays of some 1.0 and 1.7 MeV. However, we observe only one intense stretched 2639 keV $E2$ transition depopulating the 8^+ state. From the branching ratio point of view we thus have to associate the predicted 8^+_3 with the observed yrast 8^+ state. The predicted lifetime of the 7956 keV 8^+ state then amounts to $\tau = 2.4$ ps, while it was 6.2 ps for the calculated 8^+_1 level. Unfortunately, both agree with the presently available experimental knowledge. Moreover, the lifetime of the parent 10^+ shall be 6.5 ps, i.e., the γ rays below that level should not show any Doppler broadening independent from the lifetimes of the lower lying states.

3.6 Calculations and comparisons for the $N = 29$ isotones

In Fig. 15 the experimental excitation energies of the $N = 29$ isotone series ^{55}Fe [29,66], ^{56}Co [67], ^{57}Ni, and ^{58}Cu are compared to the calculated values. For ^{55}Fe a similar 'pattern' can be seen to the results in ^{54}Fe and ^{55}Co: in the low to medium spin range theory and experiment agree while at higher excitation energy the influence of the too small gap size becomes apparent as the predictions lie about 1 MeV below the observed levels. No such trend can be seen in ^{56}Co, and it is reversed for the high-spin states of the $A \geq 57$ nuclei. The (near yrast) decay pattern of both ^{55}Fe and ^{56}Co is reproduced on the same level of accuracy as, e.g., the level schemes of ^{54}Fe and ^{55}Co.

^{57}Ni was populated via the $1a2p1n$ reaction channel in our experiments. The four evaporated particles do on average not leave enough excitation energy in the residual nucleus to allow for the observation of weak branches in the high-spin regime. In turn, the still rather strong population of the reaction channel provides an extensive number of medium-spin states (and connecting γ rays) between 3 and 7 MeV excitation energy. Nevertheless, the excitation energy and its decay led us to interpret the (tentative) level at 12545 keV as the calculated $27/2^-$ state, the highest spin possible in the truncated 2h-3p model space. The 11248 keV state is thought to represent the yrast $25/2^-$ and the weakly populated 9856 and 10210 keV states the yrare $23/2^-$ levels though their feeding and decay pattern is not reproduced particularly well. This holds partly true for the cascade between the 5513 keV $15/2^-_2$ and the 9494 keV yrast $23/2^-$ state. Experimentally we observe about equally intense parallel stretched $E2$ and stretched $\Delta I = 1$ transtions. The calculations, however, clearly favor the latter. Whether or not this can be attributed to some admixed rotational collectivity arising from (moderately) deformed states is yet unclear.

The wave functions of the $17/2 \leq I \leq 23/2$ states contain hardly any partition in excess of some 20%. How-

ever, the main underlying structure is rather well established, namely the configuration $[\pi(f_{7/2})^{-1}\otimes\nu(f_{7/2})^{-1}]_7\otimes\pi(p_{3/2})$. The coupling of this structure to the remaining two neutrons in the upper fp shell and their residual interaction apparently leads to numerous final configurations which are very similar in excitation energy, and the predicted decay paths might in part strongly depend on the single-particle energies, especially for the yrare levels.

This problem is also present for the three $15/2^-$ states. In fact, the lowest calculated $15/2^-$ state contains basically no seniority $v = 3$ but solely $v = 5$ partitions with the two holes in the $1f_{7/2}$ orbit aligned to spin $I = 7$. The second $15/2^-$ state contains to a large extent the naively expected stretched $v = 3$ configurations, for example, $\nu(f_{7/2})^{-1}\otimes\nu(f_{5/2})\otimes\nu(p_{3/2})$ (23%) or $\pi(f_{7/2})^{-1}\otimes\pi(f_{5/2})\otimes\nu(p_{3/2})$ (21%). For the third $15/2^-$ state the $\nu(p_{3/2})$ is exchanged against a $\nu(f_{5/2})$ neutron. In order to get an overall better picture for the decay properties we associate the calculated yrast $15/2^-$ with the observed yrare $15/2^-_2$ state and vice versa. Nevertheless, the lifetimes of all $15/2^-$ levels are consistently predicted in the 2-10 ps range which is in agreement with the observations in, e.g, Fig 11a.

Similarly, the decay strengths from the closely neighbored yrare $7/2^-$, $9/2^-$, and $11/2^-$ states call in some cases for exchange, in other not. Yet, we decided not to interchange additional levels as it neither improves nor worsens the MBDs significantly. The yrast $3/2^-$ to $13/2^-$ states, however, are fairly stable against modifications in the single-particle energies, and their decay patterns are nicely reproduced. As in ^{56}Ni, the first 'pure' core excited $5/2^-_2$ and $7/2^-$ levels are predicted some 2 MeV too high. Since there are no major discrepancies in the decay pattern predicted for the strong transtions, a MBD=0.12(1) is achieved for a total of 29 states with known or suggested spin and parity assignments, a value similar to those of ^{54}Fe and ^{55}Co.

A final remark is mandatory with respect to the 3701 keV 9/2 level. Both this and the 3713 keV $9/2^-$ state are consistent with the predictions concerning the depopulation of the calculated yrast $9/2^-$ state. However, for none of the yrare $9/2^-$ levels a nearly exclusive decay into the 2577 keV $7/2^-$ level is predicted but instead is highly fragmented into several $9/2^-$, $7/2^-$, and $5/2^-$ states (cf. levels at 4025 and 4185 keV in Fig. 10). The sequence on top of the 3701 keV also lacks a good description with available near-yrast negative-parity states, and it is connected to those only via three weak 2-3 MeV transitions. Finally, as stated earlier, $9/2^+$ states have been observed near 3 MeV excitation energy in ^{59}Cu and ^{59}Ni [35]. In summary, there are also clues from the shell-model calculations which support the assignment of the 3701 keV 9/2 state with the neutron $1g_{9/2}$ single-particle state.

Looking at Fig. 13 the yrast decay sequence of ^{58}Cu is extremely well reproduced. The only (minor) discrepancy is the branch of the 501 keV $7^+ \rightarrow 5^+_2$ transition which experimentally amounts to 7(1)% but is predicted to be 31%. The good agreement is reflected by the small MBD of 0.09(1). The ground state has two equally strong ($\sim$ 20 %) $[\pi(p_{3/2})\otimes\nu(f_{5/2})]_1$ and $[\pi(f_{5/2})\otimes\nu(p_{3/2})]_1$ $T = 0$ components based on the respective strongly binding two-body matrix element (-3.1 MeV, [37]). The yrast 3^+ state is composed as expected, i.e., has a near 50% stretched $[\pi(p_{3/2})\otimes\nu(p_{3/2})]_3$ configuration and, also due to the low excitation energy, is predicted to have a lifetime on the order of one nanosecond. The yrast 4^+ state resembles the aligned configurations of the ground state (total 48%), while the 5^+ state is based on the aligned $[\pi(f_{5/2})\otimes\nu(f_{5/2})]_5$ (49%) configuration. Though the yrast 7^+ state contains only a 10% pure $[\pi(f_{7/2})^{-1}\otimes\nu(f_{7/2})^{-1}]_7$ partition (with the four particles in the upper fp shell coupled to spin $I = 0$) more than 70% of its wave function include the simultaneous excitation of one proton *and* one neutron across the shell gap. For the higher spin states, the four particles in the upper fp shell then gradually align their angular momenta, coupled to this 7^+ 'basis' state. The sequence finds an end at the maximum possible spin $I = 15$, and it is nicely revealed by the experimental yrast sequence with $M1$ and cross-over $E2$ transitions up the (assigned) 14^+ state at 11552 keV. The 13128 keV state would match the expected excitation energy of the 15^+ state but the discrepant decay pattern prevents a firm conclusion.

For the sake of completeness we included the $T = 1$ 0^+ and 2^+ ^{58}Ni isobaric analogue states [36] in Fig. 13b and 15. Their decay pattern and excitation energies are equally well described as the high-spin part of the level scheme.

The two 'side bands' in the experimental level scheme cannot be readily described in terms of their decay features while it should be straight forward from a purely energetic point of view (see Fig. 15). Once more, the excitation of one (or more) particles from the upper fp into the $1g_{9/2}$ orbit might cause this mismatch. Even the best scenarios for the 6793, 8126, and 9803 keV states (with tentative spin assignments) lead to large MBDs of ~ 0.3 for each of them. In contrast, the predictions for the yrare 9^+_2 state perfectly match the excitation energy and decay of the 5574 keV state through which the main portion of the γ decay out of the deformed band proceeds. Similar to the yrare 7^+_2 state its wave function is based not on 2h-4p but 1h-3p configurations. A 9^+ state, however, can also be created by fully aligning one $1g_{9/2}$ proton and one $1g_{9/2}$ neutron. The corresponding two-body matrix-element is on the order of -1.8 MeV [68,63]. Using the 3701 keV 9/2 state as a reference (which incorporates the residual interaction of one $1g_{9/2}$ particle with the ^{56}Ni core) one ends up at 2×3.7 MeV-1.8 MeV$= 5.6$ MeV for an aligned $[\pi(g_{9/2})\otimes\nu(g_{9/2})]_9$ $T = 0$ state. The experimentally observed state at 5574 keV does not only fit perfectly in energy but since it is the main collector of the γ flux from the deformed band, it should contain at least a sizeable fraction of this $g_{9/2}$ configuration.

4 Conclusions

We have presented extensive new experimental information on decay schemes in the spherical minimum of the

doubly magic nucleus ^{56}Ni and its closeby neighbours. The investigated nuclei were populated with only small fractions of the total fusion cross section, and the extraction of the comprehensive level schemes has to an extremely large extent been possible because of the use of powerful selective devices such as MICROBALL and neutron detectors. Of course, a very efficient γ-ray spectrometer such as GAMMASPHERE must form the basis of such investigations.

From the theoretical point of view, already comparatively simple shell-model calculations in the fp space and allowing up to two particles to be excited across the shell gap at particle numbers N,$Z = 28$ can succesfully describe the excitation schemes of the yrast natural parity (positive for the even-A, negative for the odd-A nuclei) schemes including the presently known electromagnetic decay properties (mainly branching ratios but also a few lifetimes and moments). The good agreement is based on the considerable lowering of the size of the gap as compared to previous studies. This leads to an artificial jump in the binding energies when crossing the gap, but the binding energies below and above the gap are within themselves well reproduced. Another consequence of the smaller gap are the relatively small (55%) closed-core partitions in the wave functions of ground-state and fully aligned configurations as well as presumed single-particle states in the $A = 57$ mirror pair. Similar scenarios are imaginable in the ^{100}Sn region where strong $E2$ $1g_{9/2}$-$2d_{5/2}$ correlations across the N,$Z = 50$ gap might have an impact on the excitation scheme or even the stability of this very exotic nucleus. Therefore, it is important to understand the experimentally more readily accessible region around ^{56}Ni in order to support predictions near ^{100}Sn.

Clearly, new experiments are neccessary to pin down the unnatural parity states and, hence, the $1g_{9/2}$ single-particle state in ^{57}Ni. Based on the present experimental and theoretical results, however, we suggest that the 3701 keV 9/2 state in ^{57}Ni is this state. Lifetime and g-factor experiments aiming at such specific states shall also provide good testing grounds for the spherical shell model in this mass region. Theoretically, the inclusion of the $1g_{9/2}$ orbit in connection with the full understanding of the comparatively weak doubly magic core certainly provides an interesting challenge.

The authors wish to thank R.M. Clark, P. Fallon, R. Krücken, I.-Y. Lee, R. MacLeod, A.O. Macchiavelli, and the operating crew of the 88-Inch Cyclotron for their assistance during this experiment. We are also indebted to D. Balamuth, S. Freeman, M. Leddy, and C.J. Lister for both providing and setting up the neutron detector array at GAMMASPHERE. Oak Ridge National Laboratory is managed by Lockheed Martin Energy Research Corp. for the U.S. Department of Energy under contract DE-AC05-96OR22464. The large body of the analysis was performed at the Ludwig-Maximilians-Universität München. This research was supported in part by the German BMBF under contract No. 06-LM-868, the Swedish Natural Science Research Councils, the U.S. Department of Energy under grant No. DE-FG02-96ER40963 (UT) and No. DE-FG05-88ER40406 (WU).

References

1. J. Huo, Nucl. Data Sheets **67**, 523 (1992)
2. D. Rudolph *et al.*, Z. Phys. **A358**, 379 (1997)
3. C.E. Svensson *et al.*, Phys. Rev. Lett. **79**, 1223 (1997)
4. D. Rudolph *et al.*, Phys. Rev. Lett. **80**, 3018 (1998)
5. C.E. Svensson *et al.*, Phys. Rev. Lett. **80**, 2558 (1998)
6. K.P. Jackson *et al.*, Phys. Lett. **33B**, 281 (1970)
7. J. Cerny and J.C. Hardy, Ann. Rev. Nucl. Sci. **27**, 333 (1977)
8. S. Åberg, P.B. Semmes, and W. Nazarewicz, Phys. Rev. **C56**, 1762 (1997)
9. C.N. Davids *et al.*, Phys. Rev. Lett. **80**, 1849 (1998)
10. D. Rudolph *et al.*, submitted to Phys. Rev. Lett
11. D. Rudolph *et al.*, Nucl. Phys. **A630**, 417c (1998)
12. I.-Y. Lee, Nucl.Phys. **A520**, 641c (1990)
13. D.G. Sarantites *et al.*, Nucl. Instrum. Meth. **A381**, 418 (1996)
14. J. Theuerkauf, S. Esser, S. Krink, M. Luig, N. Nicolay, and H. Wolters, program VS (version 6.65), Univ. of Cologne, unpublished
15. D.C. Radford, Nucl. Instrum. Meth. **A361**, 297 (1995)
16. T. Yamazaki, At. Data Nucl. Data Tables **3**, 1 (1967)
17. D.C. Camp and A.L. van Lehn, Nucl. Instrum. Meth. **76**, 192 (1969)
18. K.S. Krane, R.M. Steffen, and R.M. Wheeler, At. Data Nucl. Data Tables **11**, 351 (1973)
19. M.K. Kabadiyski, K.P. Lieb, and D. Rudolph, Nucl. Phys. **A563**, 301 (1992)
20. V. Zobel, L. Cleemann, J. Eberth, H.P. Hellmeister, W. Neumann, and N. Wiehl, Nucl. Instrum. Meth. **171**, 223 (1980)
21. J. Styczen *et al.*, Nucl. Phys. **A327**, (1979) 295
22. E. Dafni, J. W. Noé, M. H. Rafailovich, and G. D. Sprouse, Phys. Lett. **B76**, (1978) 51
23. M. H. Rafailovich, E. Dafni, J. M. Brennan, and G. D. Sprouse, Phys. Rev. **C27**, (1983) 602
24. M. Hass *et al.*, Nucl. Phys. **A414**, (1984) 316
25. J. Huo, H. Sun, W. Zhao, and Q. Zhou, Nucl. Data Sheets **68**, 887 (1993)
26. J. W. Noé, D.F. Geesaman, P. Gural, and G. D. Sprouse, Proc. Int. Conf. on Medium-Light Nuclei, Florence, Italy, 1977, eds. P. Blasi and R.A. Ricci, 458 (1978)
27. A. Schmidt, Univ. of Cologne, priv. comm
28. J. Huo, Nucl. Data Sheets **64**, 723 (1991)
29. M.G. Saint-Laurent, Sl. Cavallaro, M.L. Sperduto, B. Delaunay, J. Delaunay, and H. Dumont, Z. Phys. **A334**, 365 (1989)
30. P.M. Endt, At. Data Nucl. Data Tables **23**, 547 (1979)
31. J. Blomqvist *et al.*, Z. Phys. A **322**, 169 (1985)
32. M.R. Bhat, Nucl. Data Sheets **67**, 195 (1992)
33. K. Spohr *et al.*, Acta Phys. Pol. **B26**, 297 (1995), and K. Spohr, PhD thesis, FZ Jülich, Jül-3171, ISSN 0944-2952, 1996
34. C.E. Svensson *et al.*, to be published
35. S. Juutinen, J. Hattula, M. Jääskeläinen, A. Virtanen, and T. Lönnroth, Nucl. Phys. **A504**, 205 (1989)
36. M.R. Bhat, Nucl. Data Sheets **80**, 789 (1997)
37. W. A. Richter, M. G. van der Merwe, R. E. Julies, and B. A. Brown, Nucl. Phys. **A523** 325 (1991)

38. A. Poves and A. Zuker, Phys. Rep. **70**, 235 (1981)
39. E. Caurier, shell-model code, Strasbourg (1990)
40. E. Caurier, A.P. Zuker, A. Poves, and G. Martinez-Pinedo, Phys. Rev. **C50**, 225 (1994)
41. E. Caurier *et al.*, Phys. Rev. Lett. **75**, 2466 (1995)
42. G. Martinez-Pinedo *et al.*, Phys. Rev. **C54**, R2150 (1996)
43. S. Lenzi *et al.*, Z. Phys. **A354**, 117 (1996)
44. S. Lenzi *et al.*, Phys. Rev. **C56**, 1313 (1997)
45. C.A. Ur *et al.*, Phys. Rev. **C**, in press
46. S.E. Koonin, D.J. Dean, and K. Langanke, Phys. Rep. **278**, 1 (1996), and references therein
47. M. Honma, T. Mizusaki, and T. Otsuka, Phys. Rev. Lett. **75**, 1284 (1995)
48. M. Honma, T. Mizusaki, and T. Otsuka, Phys. Rev. Lett. **77**, 3315 (1996)
49. K. Langanke *et al.*, Nucl. Phys. **A613**, 253 (1997)
50. T. Otsuka, M. Honma, and T. Mizusaki, Phys. Rev. Lett., in press
51. T. Otsuka, priv. comm
52. D. Zwarts, Phys. Comm. **38**, 365 (1985)
53. L. Trache *et al.*, Phys. Rev. **C54**, 2361 (1996)
54. A.P. Zuker, J. Retamosa, A. Poves, and E. Caurier, Phys. Rev. **C52**, R1741 (1995)
55. B.A. Brown, priv. comm
56. G. Martinez-Pinedo *et al.*, Phys. Rev. **C55**, 187 (1997)
57. A.K. Dhar and K.H. Bhatt, Phys. Rev. **C16**, 792 (1977)
58. P. Raghavan, M. Senba, Z.Z. Ding, A. Lopez-Garcia, B.A. Brown, and R.S. Raghavan, Phys. Rev. Lett. **54**, 2592 (1985)
59. G. Audi and A.H. Wapstra, Nucl. Phys. **A565**, 1 (1993); Nucl. Phys. **A595**, 409 (1995)
60. P. Raghavan, At. Data Nucl. Data Tables **42**, 189 (1989)
61. T. Ohtsubo, D.J. Cho, Y. Yanagihashi, S. Ohya, and S. Muto, Phys. Rev. **C54**, 554 (1996)
62. S.S. Rosenbaum and W.A. Steyert, Phys. Lett. **55B**, 450 (1975)
63. D. Rudolph, K.P. Lieb, and H. Grawe, Nucl. Phys. **A597**, 298 (1996)
64. S. Frauendorf, Nucl. Phys. **A557**, 259c (1993)
65. G. Kraus *et al.*, Phys. Rev. Lett. **73**, 1773 (1994)
66. H. Fromm *et al.*, J. Phys. **G7**, L109 (1981)
67. M. Palacz *et al.*, Nucl. Phys. **A627**, 162 (1997)
68. R. Gross and A. Frenkel, Nucl. Phys. **A267**, 85 (1976)